



Saline fluids drive Cu mineralization in Precambrian metasediments: Evidence from the Trans-North China Orogen

Zheng-Jie Qiu^{a,b}, Hong-Rui Fan^{a,b,c,*}, M. Santosh^{d,e}, Kui-Feng Yang^{a,b,c}, Xiao-Chun Li^{a,b,c}, Ting-Guang Lan^{c,f}, Yan-Wen Tang^f, Yong-Xin Pan^{b,c}

^a Key Laboratory of Mineral Resources, Institute of Geology and Geophysics, Chinese Academy of Sciences, Beijing 100029, China

^b Innovation Academy for Earth Science, Chinese Academy of Sciences, Beijing 100029, China

^c College of Earth and Planetary Sciences, University of Chinese Academy of Sciences, Beijing 100049, China

^d School of Earth Sciences and Resources, China University of Geosciences Beijing, Beijing 100083, China

^e Department of Earth Science, University of Adelaide, Adelaide, SA 5005, Australia

^f State Key Laboratory of Ore Deposit Geochemistry, Institute of Geochemistry, Chinese Academy of Sciences, Guiyang 550081, China

ARTICLE INFO

Keywords:

Epigenetic hydrothermal Cu deposit
LA-ICP-MS fluid inclusion analysis
Metamorphic brine
Trans-North China Orogen

ABSTRACT

Epigenetic hydrothermal Cu(Co) deposits are widely distributed in the Zhongtiao Mountains within the Paleoproterozoic Trans-North China Orogen in the North China Craton. Here we investigate the Henglingguan Cu deposit hosted in metasediments to gain insights on the fluid evolution characteristics associated with the ore formation. This Cu deposit is characterized by early disseminated mineralization and late quartz-vein type mineralization. The negative sulfur isotope values (about -10%) of the vein sulfides suggests a sedimentary rock source for sulfur associated with the hydrothermal Cu mineralization. The coexistence of CO_2 -rich carbonic inclusions and halite-bearing inclusions within a single fluid inclusion assemblage suggests fluid immiscibility in the H_2O -NaCl- CO_2 system. Based on the fluid phase analysis, our data show that the parent ore fluid was characterized by X(NaCl) of 10 to 20 mol.% (salinity of around 23 to 41 wt% NaCl) and X(CO_2) of 10 to 15 mol.% before fluid immiscibility. The estimated temperature–pressure conditions of 320 to 340 °C and 3.5 to 4.0 kbar based on the carbonic fluid inclusions is suggested to be close to the conditions of fluid immiscibility. *In-situ* composition analyses of fluid inclusions by LA-ICP-MS show that the ore fluids contained Na, Ca, Fe and Mn, and evolved towards Sr-Ba enrichment. The data are consistent with a metamorphic brine derived from the sedimentary rocks. The brine-rich metamorphic fluids were likely derived from the dehydration and decarbonation of evaporitic carbonate rocks developed on the basin margin or a passive continental margin. The decompression during post-collisional exhumation triggered fluid immiscibility resulting in the quartz vein-type Cu mineralization.

1. Introduction

Chloride-rich crustal fluids have a great ability to transport metals and to form epigenetic hydrothermal ore deposits at ductile–brittle transition zones within the crust (Groves and Bierlein, 2007; Yardley and Cleverley, 2015; Zhong et al., 2015; Hammerli and Rubenach, 2018; Morrissey and Tomkins, 2020; Qiu et al., 2021a). The orogenic gold deposits are genetically linked to metamorphic fluids characterized by low salinity, near-neutral, aqueous carbonic fluids (Ridley and Diamond, 2000; Groves et al., 2003; Goldfarb et al., 2005; Phillips and Powell, 2010). The solubility of ore metals including Cu, Pb, Zn, Co, and

Ni is strongly enhanced by the presence of Cl in the hydrothermal fluids (e.g., Seward et al., 2014; Brugger et al., 2016). However, the source of saline ore fluids in epigenetic hydrothermal Cu-Co deposits within metamorphic terranes is still unclear (Oliver, 1996; Selley et al., 2005; Sillitoe et al., 2017). Saline crustal fluids can be produced by: (1) magmatic fluids exsolved from crystallizing plutons (e.g., Heinrich and Candela, 2014), (2) downward circulation of basinal brines into basement rocks (e.g., Oliver, 1996), (3) mobilization of an originally saline connate fluid or dissolution of salts of sedimentary origin (e.g., Warren, 2016), and (4) release from evaporite rocks during metamorphic dehydration reaction (e.g., Morrissey and Tomkins, 2020; Qiu et al.,

* Corresponding author at: Key Laboratory of Mineral Resources, Institute of Geology and Geophysics, Chinese Academy of Sciences, Beijing 100029, China.
E-mail address: fanhr@mail.iggcas.ac.cn (H.-R. Fan).

2021a).

The genetic association between hydrothermal ore deposits and magmas is well studied and documented in several studies of mineralization close to magmatic intrusions and through modeling the fluid evolutions (e.g., Heinrich, 2005; Sillitoe, 2010). Some epigenetic hydrothermal Cu deposits have been confirmed to be associated with the metamorphism, such as *syn*-tectonic breccia-hosted Mount Isa Cu deposits, Queensland, Australia (Gregory et al., 2008), metasedimentary rock hosted Cu-U deposits in the Pan-African Lufilian orogenic belt (Turlin et al., 2016; Eglinger et al., 2016). It is important to be able to distinguish between magmatic fluids related to granitoid intrusions from those metamorphic fluids released by prograde metamorphic dehydration reactions in the low to middle crust depth. The fluid sources of metasedimentary rock-hosted Cu deposits are debated, and detailed fluid compositional data are lacking, particularly the detailed information on major and trace element composition of the ore-forming fluids through laser ablation-inductively coupled plasma-mass spectrometry (LA-ICP-MS) of individual inclusions (Rusk et al., 2004; Large et al., 2016).

In this contribution, we present results from our study on the Henglingguan Cu deposit in the Zhongtiao Mountains district within the Paleoproterozoic Trans-North China Orogen (TNCO) in the North China Craton. The pressure-temperature-composition conditions of the ore-forming fluids are addressed through a detailed fluid inclusion microthermometry, laser Raman microspectrometry, and *in-situ* LA-ICP-MS analyses of fluid inclusions. Our data are useful to constrain the genetic model of the metasedimentary rock-hosted Cu deposit and further highlight the important role of the metamorphic brines in the process of ore transportation and mineralization.

2. Geologic setting

2.1. Regional geology

The North China Craton (NCC), comprising the Eastern and Western blocks, is separated by the TNCO, representing a major Paleoproterozoic collisional orogen (e.g., Zhao et al., 2005; Tang and Santosh, 2018). This orogenic belt is mainly composed of voluminous Neoproterozoic to Paleoproterozoic tonalite-trondhjemite-granodiorite gneisses, granulites, granitoids, metavolcanic-sedimentary rocks (e.g., Zhai and Santosh, 2013), and records a complete history of rifting followed by collision from 2.25 to 1.85 Ga (e.g., Zhai and Santosh, 2013; Tang and Santosh, 2018).

The medium to large Cu deposits are hosted in the southern section of the TNCO, within the Zhongtiao Mountains district (Fig. 1a). In this Cu district, the Paleoproterozoic (~2.2 to 2.1 Ga) supracrustal rocks are subdivided into the Jiangxian, Zhongtiao, Danshanshi, and Xiyang Groups (Fig. 1a). The basal Jianxian Group is a thick sequence of volcano-sedimentary rocks, and are further subdivided into the basal Henglingguan subgroup, comprising of a thin layer of quartzite and mica-schist, and the upper Tongkuangyu subgroup, including quartzite, pelitic schist, *meta*-basic volcanic rocks, *meta*-tuff, and *meta*-rhyolite. The sedimentation timing is estimated as 2.16–2.19 Ga based on zircon geochronology on the intercalated amphibolite from this group (Liu et al., 2015). The Tongkuangyu deposit, the largest Cu deposit at Zhongtiao Mountains, is located in the Tongkuangyu subgroup and is associated with *meta*-volcanic rocks and granitic intrusions. The Tongkuangyu deposit is interpreted as an ancient porphyry-type deposit (e.g., Jiang et al., 2014; Meng et al., 2020). The host mafic volcanic rocks and granitic rocks intruded at ca. 2.2 Ga, revealed by zircon U-Pb dating (Liu et al., 2015). Liu et al (2019) stressed that copper mineralization and

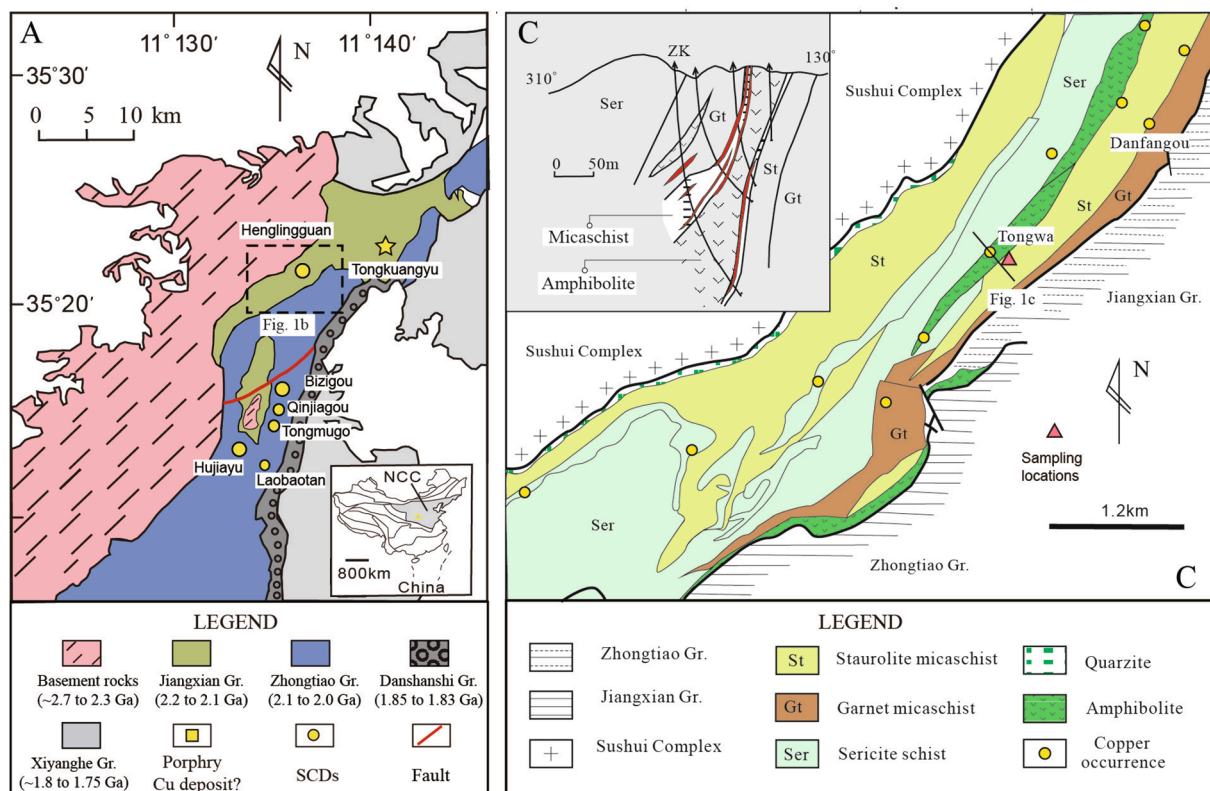


Fig. 1. (A) Simplified geological map of the Zhongtiao Mountains district (Modified from Qiu et al., 2016). (B) Geological map of the Henglingguan metasedimentary rock hosted Cu-(Co) deposits in the Henglingguan Formation, Jiangxian Group (modified from Hu and Sun, 1987). (C) Geological section of the Tongwa orebody, one of the typical Cu-(Co) orebodies in the Henglingguan deposit (modified from Hu and Sun, 1987). Abbreviations: ZK = Drill hole; Fm. = Formation; Gr. = Group; St = staurolite; Gt = Garnet; Ser = sericite; Amp = amphibolite.

remobilization formed during metamorphic retrogression. The hydrothermal remobilization was constrained at 1.9–1.8 Ga (Liu et al., 2019; Meng et al., 2020). Some small Cu deposits also occur in the basal Henglingguan subgroup. The Zhongtiao Group with thick clastic-pelitic-carbonate sedimentary sequence unconformably covers the Jiangxian Group. This group comprises quartzite, meta-sandstones, pelitic schist, thick marble, and minor meta-volcanic rocks. The sedimentary sequence is interpreted to have been deposited during transgression events along the continental margin (Hu and Sun, 1987). Zircon U-Pb ages of the interlayered metavolcanic rocks constrain the deposition at ~ 2.1 Ga (Sun et al., 1990; Liu et al., 2015). Several medium sized of metasedimentary rock-hosted Cu-Co deposits are also located in the Zhongtiao group (Qiu et al., 2015). The orebodies are mainly hosted in the graphite schist and dolomitic marble. The disseminated-veinlet mineralization in these deposits was interpreted to have formed during the metamorphic peak and the major hydrothermal vein-type mineralization occurred during the retrograde cooling (Qiu et al., 2016).

The Jiangxian and Zhongtiao Group were subjected to upper greenschist to amphibolite facies regional metamorphism (550–650 °C, 5–7 kbar) (Qiu et al., 2017). The Danshanshi Group is composed of low-grade metamorphic conglomerates and sandstones (Sun et al., 1990). The Jiangxian Group, a Mesoproterozoic unit of unmetamorphosed basaltic andesite, unconformably cover the Paleoproterozoic sedimentary sequences. The detailed regional geology of the Zhongtiao Mountains district is summarized by Liu et al. (2016) and Qiu et al. (2016).

2.2. The Henglingguan Cu deposit

The Henglingguan Cu deposit is hosted in the Henglingguan Formation of the Jiangxian Group and at least ten Cu occurrences have been identified (Fig. 1b). This deposit is classified as a metasedimentary rock-hosted Cu deposit (e.g., Hu and Sun, 1987), or also termed as mica-schist-hosted Cu deposit (Qiu et al., 2017). The orebodies are mainly hosted in the mica-schist (Fig. 2a) and partly associated with amphibolite. One of the typical geological sections of the orebody is shown in Fig. 1c. The wall rock is mica-schist (Fig. 2a). A previous study on mineral geothermobarometry work and P-T pseudosection analysis of the host staurolite mica schist and garnet-bearing amphibolite rocks revealed prograde metamorphism from 565 to 595 °C, and peak metamorphism of ~ 6.5 kbar and ~ 610 °C (Qiu et al., 2017). Two stages of mineralization are identified in the ore samples: disseminated mineralization (Fig. 2b, d) and foliation-parallel quartz-sulfide veinlet to vein mineralization (Fig. 2c, e, and f). The ore-forming process of the Henglingguan deposit was suggested to be synchronous with regional

metamorphism based on the detailed petrological, mineralogical and geochronological study (Qiu et al., 2017). The disseminated mineralization (M-1), consisting of chalcopyrite, pyrite, and some cobaltite was likely to form through metamorphic overprinting on diagenetic sulfides (Qiu et al., 2017). The vein-type mineralization corresponds to epigenetic hydrothermal mineralization formed during retrograde metamorphic stage or orogenic uplift stage based on the geochronological and geothermometric results (Qiu et al., 2017). The available age data suggests peak metamorphism happened at ~ 1881 Ma based on U-Pb dating of metamorphic monazites in the mica-schist, and the hydrothermal mineralization age was estimated at ~ 1863 Ma by U-Pb dating of hydrothermal monazites from the quartz veins. The epigenetic hydrothermal mineralization was constrained at ~ 450 °C from arsenopyrite thermometer, and ~ 350 °C and ~ 4.4 kbar from sphalerite geothermobarometer (Qiu et al., 2017). A clockwise Franciscan type P-T-t path has been inferred, suggesting crustal thickening followed by a sluggish exhumation in a collisional environment (Qiu et al., 2017).

3. Analytical techniques

3.1. Sulfur isotope analysis of sulfides by LA-ICP-MS

Sulfur isotope analyses of sulfides were conducted using a Nu Plasma II MC-ICP-MS equipped with a RESOLUTION S-155 193 nm excimer ArF laser ablation system at the State Key Laboratory of Geological processes and Mineral Resources, China University of Geosciences (Wuhan). The laser ablation spot was set to 33 µm in diameter, with a pulse energy density of 3–4 J/cm² and a repetition rate of 8 Hz. The analytical session for each spot was 65 s, comprising a 25 s measurement of background and a 40 s sample analysis. Sample-standard bracketing was implemented to correct for instrumental mass bias and drift throughout the analytical sessions. An in-house pyrite natural standard WS-1 (Zhu et al., 2016), was used to calibrate the S isotopes. These standards were measured after every five to eight sample spots. Measured sulfur isotope ratios of sulfides were normalized by WS-1 compositions (1.1 ‰ ± 0.2 ‰, Zhu et al., 2016), then corrected for the instrumental mass fractionation factor. For in-situ sulfur isotopic analysis of sulfate, the operation parameter was set to 33 µm in diameter, with a pulse energy density of 6–8 J/cm² and a repetition rate of 12 Hz. Measured sulfur isotope ratios of barite were normalized by YF-2 barite with a referred δ³⁴S value of 18.1 ‰ ± 0.4 ‰ (Lu et al., 2021). In this study, analytical precision for δ³⁴S values is reported at the 1σ confidence level (1SD = 0.2 ‰). Sulfur isotopic compositions of sulfides and barite are summarized in Table 1.

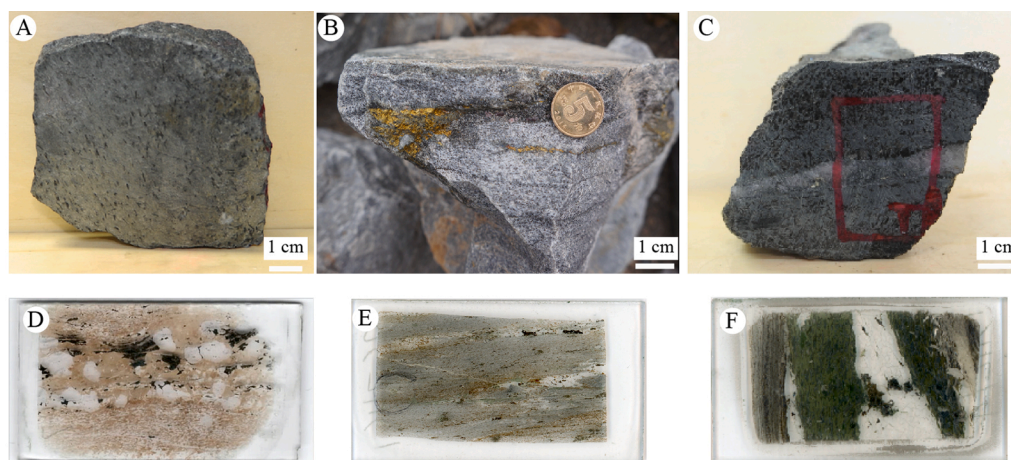


Fig. 2. Photos of host rocks and ore samples in the Tongwa orebody in the Henglingguan deposit. (A) Sericitization mica schist. (B) Disseminated mineralization in mica schist. (C) Quartz-sulfides veins mineralization. The scanning of petrographic thin sections of disseminated Cu mineralization within the garnet-biotite assemblages (D), foliation-parallel quartz veinlet mineralization (E), and quartz vein mineralization (F).

Table 1*In-situ* LA-MC-ICPMS sulfur isotope data for sulfides and barite in the Henglingguan Cu deposit, Zhongtiao Mountains district.

Analysis No.	Mineral	$\delta^{34}\text{S}$	Analysis No.	Mineral	$\delta^{34}\text{S}$	Analysis No.	Mineral	$\delta^{34}\text{S}$
Foliation-parallel quartz-sulfides veinlets Py-Po-Apy-Cpy assemblage								
15HL90-1	Cpy	-9.9	15HL90-12	Py	-10.8	15HL90-9	Apy	-9.4
15HL90-2	Cpy	-9.7	15HL90-13	Py	-10.9	15HL90-10	Apy	-9.4
15HL90-3	Cpy	-9.9	15HL90-14	Py	-10.8	15HL90-11	Apy	-9.0
15HL90-4	Cpy	-10.3	Average		-10.8	Average		-9.3
15HL90-5	Cpy	-10.2	SD		0.1	SD		0.2
15HL90-6	Cpy	-10.5	15HL90-15	Po	-9.9	15HL90-20	Apy	-7.6
15HL90-7	Cpy	-10.1	15HL90-16	Po	-10.2	15HL90-21	Apy	-7.6
15HL90-8	Cpy	-10.0	15HL90-17	Po	-10.3	15HL90-22	Apy	-7.1
			15HL90-18	Po	-10.2	15HL90-23	Apy	-8.9
			15HL90-19	Po	-10.2	15HL90-24	Apy	-7.5
			Average		-10.2	15HL90-25	Apy	-8.6
			SD		0.1	15HL90-26	Apy	-7.6
Average		-10.1				Average		-7.9
SD		0.3				SD		0.7
Foliation-parallel quartz-sulfides veinlets Cpy-Py - Brt assemblage								
15HL55-01	Cpy	-14.4	15HL55-06	Py	-14.8	15HL55-B02	Brt	-4.2
15HL55-02	Cpy	-14.7	15HL55-07	Py	-14.9	15HL55-B04	Brt	-6.2
15HL55-03	Cpy	-14.8	15HL55-08	Py	-14.8	15HL55-B05	Brt	-2.0
15HL55-04	Cpy	-14.3	15HL55-09	Py	-14.7	Average		-4.2
15HL55-05	Cpy	-14.1	15HL55-10	Py	-14.3	SD		2.1
Average		-14.5	Average		-14.7			
SD		0.3	SD		0.3			
Lentoid quartz-sulfides veins with Cpy-Py assemblage								
13HL21-1	Cpy	-10.8	13HLY4-1	Cpy	-11.1	13HLY4-6	Py	-10.7
13HL21-2	Cpy	-11.1	13HLY4-2	Cpy	-11.5	13HLY4-7	Py	-11.9
13HL21-3	Cpy	-11.1	13HLY4-3	Cpy	-11.5	13HLY4-8	Py	-11.5
13HL21-4	Cpy	-10.9	13HLY4-4	Cpy	-11.7	13HLY4-9	Py	-10.0
13HL21-5	Cpy	-10.7	13HLY4-5	Cpy	-11.3	13HLY4-10	Py	-10.7
Average		-10.9	Average		-11.4	Average		-11.0
SD		0.2	SD		0.2	SD		0.8

3.2. Laser Raman spectrometry

Non-destructive analyses of the compositions of gas and solids in fluid inclusion were conducted on a HORIBA Jobin Yvon LabRam HR laser Raman spectrometer at the Institute of Geology and Geophysics, Chinese Academy of Sciences (IGGCAS). The Torus 532 laser with a wavelength of 532 nm and a source power of 44 mW was used in the analysis. The vapor phase was scanned in three ten-second cycles within the spectral range of 1000 to 4000 cm^{-1} . The solids were scanned in three ten-second cycles within the spectral range of 100 to 4000 cm^{-1} .

3.3. Fluid inclusion microthermometry

Samples of sulfide-quartz veinlets and veins were prepared as 0.2–0.3 mm thick doubly polished plates. After a detailed fluid inclusion petrographic study, representative fluid inclusions were selected for microthermometry, using a Linkam THMSG 600 programmable heating-freezing stage combined with a Zeiss microscope at IGGCAS. The stage was calibrated using synthetic fluid inclusions supplied by FLUID INC. through calibration against the triple-point of pure CO_2 (-56.6°C), the freezing point of water (0.0°C), and the critical point of water (374.1°C). Most measurements were carried out at a heating rate of 0.2 to 0.4 $^\circ\text{C}/\text{min}$. Carbonic phase melting ($T_m\text{-CO}_2$) and clathrate melting ($T_m\text{-clath}$) were determined by temperature cycling (Diamond, 2001; Fan et al., 2003). The heating rate for measurements was reduced to 0.1–0.2 $^\circ\text{C}/\text{min}$ near phase transformations. The precision of measurements was $\pm 0.2^\circ\text{C}$ at temperatures below 30°C and $\pm 2^\circ\text{C}$ at temperatures above 30°C . The fluid inclusion assemblage (FIA) method was used in the fluid inclusions study. An FIA is a group of co-genetic fluid inclusions occupying an individual petrographic feature (crystal growth zone, planar array or healed fracture) by a single event (Goldstein and Reynolds, 1994; Goldstein, 2001; Chi et al., 2021).

Fluid salinities, densities, bulk compositions, and isochores of CO_2 -rich inclusions and aqueous fluid inclusions were calculated using the FLUID software package of Bakker (2003). Isochores were calculated

using the equation of Sterner and Bodnar (1991) for $\text{CO}_2\text{-H}_2\text{O}$ inclusions. Salinities, densities, and isochores of the inclusions that homogenize by halite dissolution were calculated with the equations proposed by Lecumberri-Sanchez et al. (2012).

3.4. Composition analysis of single fluid inclusions by LA-ICP-MS

Major and trace element analyses of single fluid inclusions from the quartz veins were conducted on an Agilent 7900 ICP-MS equipped with a GeoLasPro 193 nm ArF excimer laser at the State Key Laboratory of Ore Deposit Geochemistry, Institute of Geochemistry, Chinese Academy of Sciences. The instrument setting conditions are the same as the description from Lan et al. (2018). Laser repetition of 10 Hz and energy density of 10 J/cm^2 were used during the analyses. Laser spot sizes were adjusted from 16 to 44 μm for the fluid inclusion analyses. For fluid inclusion major and trace element calibrations, the raw LA-ICP-MS data were reduced using the SILLS software (Guillong et al., 2008). NIST SRM610 was used as an external standard and analyzed twice every 10 analyses. The equivalent wt.% NaCl concentrations in the fluid inclusions, which were obtained independently from the microthermometry, were used as the internal standard (Heinrich et al., 2003). The charge-balance method was adopted to correct the modeled amounts of Na (from the wt. % NaCl equiv.) for salinity contributions of other chloride salts (Allan et al., 2005).

4. Results

4.1. Ore petrography and paragenesis

Our fieldtrip investigations and petrographic observation revealed three types of mineralization at Henglingguan. The mineral paragenesis is summarized in Fig. 4. The disseminated chalcopyrite, pyrite, and cobaltite formed in the main metamorphic stage, whereas the epigenetic vein-type hydrothermal mineralization developed at the late retrogressive metamorphic stage.

The early stage of disseminated mineralization (M-1) is dominantly represented by massive chalcopyrite, occurring in between garnet and biotite or occurring as inclusions in the garnet (Fig. 2d). Minor pyrite and cobaltite also occur at this stage. The coexistence of disseminated sulfides and metamorphic minerals indicates the presence of Fe-Cu-Co-Ni-S in the protolith of mica schist before metamorphism.

The late stage of vein-type mineralization is further divided into quartz veinlet type mineralization (M-2) and quartz vein type mineralization (M-3). The quartz veinlet type mineralization is composed of bornite-chalcopyrite-barite (Bn-Cpy-Brt) assemblage (Fig. 3d) and chalcopyrite-pyrrhotite-arsenopyrite-pyrite (Cpy-Po-Apy-Py) assemblage (Fig. 3a-c). The quartz vein type mineralization is the main Cu mineralization stage, characterized by chalcopyrite-pyrite-sphalerite (Cpy-Py-Sph) assemblage in the lenticular quartz veins (Fig. 3e-f). All these veins are parallel to the host-rock foliations (Fig. 2e-f). Based on the previous mineral geothermometry estimate (Qiu et al., 2017), the Cpy-Po-Apy-Py assemblage with a high temperature of ~ 450 °C formed earlier than the Cpy-Py-Sph assemblage with an estimated temperature of ~ 350 °C.

4.2. Sulfur isotopic compositions of sulfides

The *in-situ* sulfur isotope analysis was focused on epigenetic hydrothermal sulfides. In the Cpy-Po-Apy-Py assemblage (Fig. 3a-c), chalcopyrite, pyrrhotite and pyrite have similar sulfur isotope compositions with $\delta^{34}\text{S}$ values of -9.7 to -10.0 ‰ (average at -10.1 ± 0.3 ‰, $n = 8$), -9.9 to 10.3 ‰ (-10.2 ± 0.1 ‰, $n = 5$), and -10.8 to -10.9 ‰ (-10.8 ± 0.1 ‰, $n = 3$), respectively. Arsenopyrite in this assemblage has relatively high $\delta^{34}\text{S}$ values of -9.0 to -9.4 ‰ (-9.3 ± 0.2 ‰, $n = 3$) and -7.1 to -8.9 ‰ (-7.9 ± 0.7 ‰, $n = 7$). In the Cpy-Py-Brt assemblage (Fig. 3d), chalcopyrite and pyrite have $\delta^{34}\text{S}$ values of -14.1 to -14.8 ‰ (-14.5 ± 0.3 ‰, $n = 5$) and -14.3 to 14.9 ‰ (-14.7 ± 0.3 ‰, $n = 5$). Barite is rich in ^{34}S ranging from -6.2 to -2.0 ‰ with an average of -4.2 ± 2.1 ‰ ($n = 3$). In the Cpy-Py-bearing quartz veins (Fig. 3e and f), chalcopyrite and pyrite have $\delta^{34}\text{S}$ values of -10.7 to -11.7 ‰ and -10.0 to 11.9 ‰. The sulfur isotope fractionation between sulfides (Py-Cpy-Po) is insignificant within the 2 standard deviation error (~ 0.4 ‰) of sulfur isotope analysis (Fig. 5a and b). No available sulfur isotope equilibration temperature is obtained. The sulfur isotope fractionation between chalcopyrite and barite is large with a variable range of 8.6 to 12.8 ‰ and yielded a temperature range of 600 to 500 °C with less confidence (Fig. 5e).

Mineralization stage	Metamorphism	Epigenetic hydrothermal mineralization	
	M1 Disseminated	M2 Quartz veinlets	M3 Quartz veins
Garnet	█		
Staurolite	█		
Muscovite	█		
Biotite	█		
Chlorite	█	█	
Quartz	█	█	█
Calcite		█	
Cobaltite	█		
Chalcopyrite	█	█	█
Pyrite		█	
Bonite		█	
Barite		█	
Pyrrhotite		█	
Arsenopyrite		█	
Sphalerite			█

Fig. 4. Mineral paragenetic sequence of the Henglingguan sedimentary rock hosted Cu deposit. The width of solid bars correlates to mineral abundance.

4.3. Fluid inclusion petrography and microthermometric results

To better constrain the compositions and P-T conditions of ore fluids, we focused on the copper-bearing quartz veins from the Henglingguan deposit. The fluid inclusions located in the planar arrays or the healed fractures within a single quartz grain were selected for microthermometric work. The microthermometric results of fluid inclusion assemblages (FIAs) are listed in Supplementary Table S1 and summarized in Table 2.

Four types of fluid inclusion assemblage (FIA) were identified based on the type or combination of types of fluid inclusions within the FIA (Figs. 6a-d and 7). The characteristics of each type of FIA (i.e., type-I to type-IV FIAs) are described below.

The type-I FIA consists of a mixture of halite-bearing inclusions (type S), aqueous-carbonic inclusions (type AC) and occasionally halite-bearing carbonic inclusions (type HC). These different types of inclusion are considered to be entrapped at the same time. These FIAs occur in clean quartz grains enclosed in massive chalcopyrite (Fig. 6a), and

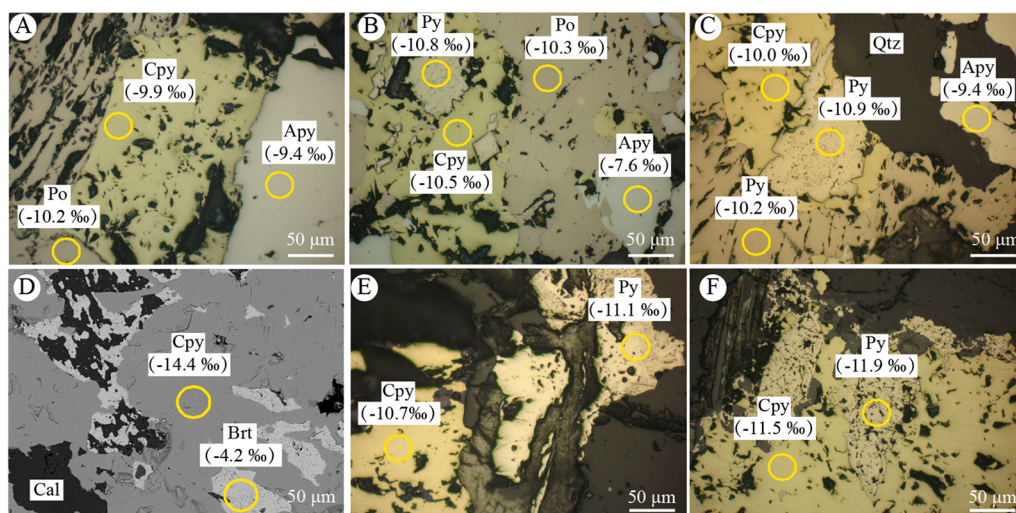


Fig. 3. Representative photomicrographs of mineral assemblages in ore samples and host rocks. (A-C) Reflected light images of pyrite-chalcopyrite-pyrrhotite-arsenopyrite assemblage in the foliation-parallel quartz-sulfides veinlets. (D) BSE image of pyrite-chalcopyrite-barite assemblage in the foliation-parallel quartz-calcite veinlets. (E-F) Reflected light images of pyrite-chalcopyrite assemblage in the lenticular quartz-sulfides veins. Abbreviations: Apy-arsenopyrite, Brt-barite, Cal-calcite, Cpy-chalcopyrite, Py-pyrite, Qtz-quartz.

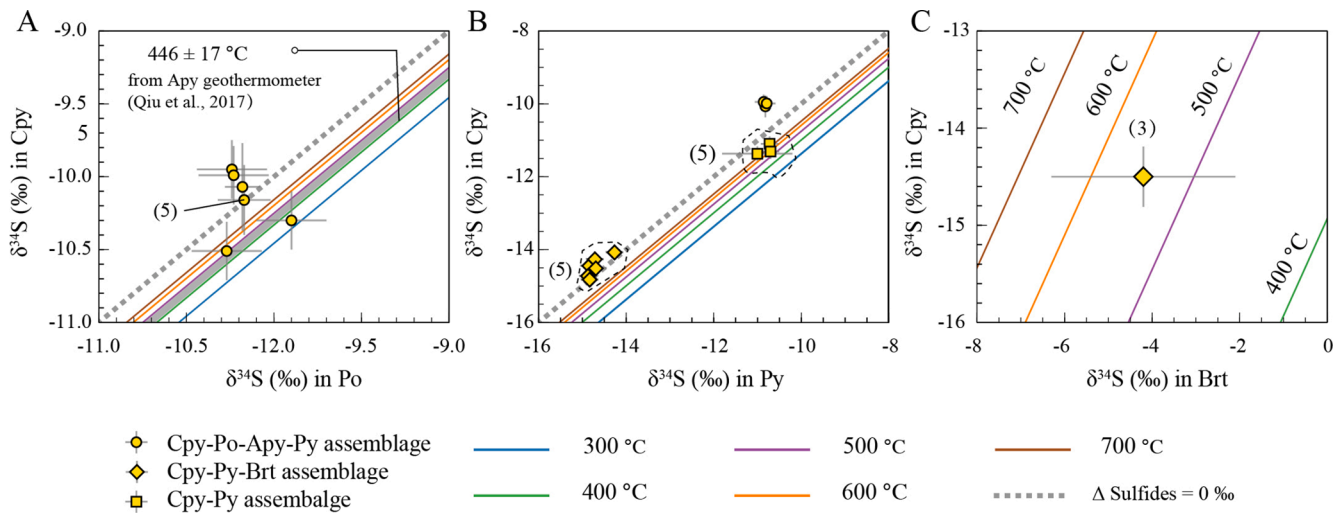


Fig. 5. Plots of $\delta^{34}\text{S}$ of chalcopyrite versus pyrrhotite (A), barite (B), and pyrite (C) in hydrothermal veinlet-veins. The different shapes of symbols are for different veins. The colored solid lines are theoretical aspects of equilibrium fractionation of sulfur isotopes between sulfides and sulfate at specific temperatures.

Table 2

Summary of microthermometric results for 4 types of fluid inclusion assemblage (FIA) from copper-bearing quartz veins in the Henglingguan Cu deposit.

FIA types	Type I			Type-II	Type-III	Type-IV
Fluid inclusion type	CO ₂ -H ₂ O inclusions (type AC)	Halite-bearing (type S)	Halite-bearing carbonic inclusion (type HC)	Halite-bearing (type S)	CO ₂ -H ₂ O inclusions (type AC)	Biphase aqueous (type A)
Aqueous liquid %	10 to 30	60 to 75	20 to 40	50 to 60	10 to 25	85 to 90
T _{fm} , °C	-59 to -56.6	-28 to -25	-	-28 to -22	-60 to -56.6	-23 to -21
T _{m(ice)} , °C	-	-	-	-	-	-1.8 to -6.8
T _{clath}	-	-	-	-	-	-
Th(CO ₂), °C	-5.2 to -10.5	-	-	-	-3.4 to -9.3	-
Mode	Carbonic vapor disappears	-	-	-	Carbonic vapor disappears	-
Th(V-L), °C	280 to 350	143 to 280	280 to 320	100 to 220	320 to 340	90 to 230
Mode	Carbonic liquid	Aqueous liquid	Decrepitated	Aqueous liquid	Carbonic liquid	Aqueous liquid
T _{m(halite)}	N.O.	190 to > 600	-	135 to > 550	-	-
Salinity (wt.% NaCl)	-	31.2 to 55.0	-	31.0 to 54.2	-	3.1 to 9.1
X (H ₂ O), %	10 to 40	28 to 59	-	27 to 55	22 to 44	88 to 94
X (NaCl), %	0	41 to 72	-	38 to 73	0	6 to 12
X (CO ₂), %	60 to 90	0	-	0	56 to 78	-
Bulk density (g/cm ³)	0.95 to 0.99	1.14 to 1.52	-	1.17 to 1.60	0.95 to 1.01	0.97 to 0.99

Aqueous liquid %: the percentage of aqueous liquid at room condition; T_{fm}: the first melting temperature; T_{clath}: clathrate melting temperature; Th(CO₂): homogenization temperature of carbonic phase; Mode: mode of homogenization to liquid phase (L) or vapor phase (V); T_m (halite): the melting temperature of halite.

does not have secondary cracks. The type-I FIA also occur as cluster next to a healed trail (Fig. 6b). The occurrence of type HC inclusion further supports that the carbonic fluid and brine fluid were entrapped simultaneously, suggesting a heterogenous entrapment. Many of these inclusions underwent necking down phenomenon (Fig. 6a). For example, the inclusion image with the number of 3 in Fig. 6a shows a tiny halite crystal in the inclusion tail. The inclusion shown as number 4 in Fig. 6a shows an aqueous inclusion next to an including carrying a halite crystal. Type AC inclusions from this type-I FIA are commonly in rounded or negative crystal shapes with sizes of 8–15 μm . The carbonic phase occupies 70 to 90 vol%, and the remaining is aqueous phase. On cooling runs, most type AC inclusions were frozen to solid at -100 to -110 °C. On heating runs, the first melting temperatures are closing to -56.6 °C. The partially homogenization temperatures of the liquid carbonic phase are in the range of -5.2 to -10.5 °C and totally homogenization into the one phase (aqueous phase disappears) occurs at the temperatures of 280 to 350 °C. The type S inclusions have variable sizes of halite solids. Halite dissolved at the wide temperature range of 190° to 560 °C, while some larger halite crystals and did not dissolve

even above 600 °C. The salinities of type S inclusions are best constrained at the range of 31 to 55 wt% NaCl equiv. (Table 2).

The type-II FIA consists of halite-bearing inclusions (type S) occurring in planar arrays (Fig. 6c) or healed trails (Fig. 6d). Type S inclusions are in irregular or elliptical in shape, with diameters of 8–15 μm , containing a cubic halite crystal and a small vapor bubble, or some other subrounded solids at times (Fig. 6e). Halite was inferred from its shape and refractive index similar to that of an aqueous liquid. The sizes of the halite crystals are highly variable, and some of them almost occupy more than half of the volume of the inclusions. Subrounded solid grains in type S inclusions were identified as calcite crystals by Raman analyses (Fig. 8b). The vapor bubble in type S inclusions disappeared at the temperature range of 145 to 200 °C. Halite dissolved at the temperature range of 210 to 350 °C. All the calcite grains did not dissolve during the heating run. The salinities are constrained at the range of 31 to 54 equiv. wt. % NaCl (Table 2). In the liquid–vapor homogenization temperature (Th) - halite dissolution temperature (Tm) diagram (Fig. 9b), type S inclusions are characterized by variable Tm values, but with a narrow range of Th values of 143° to 185 °C.

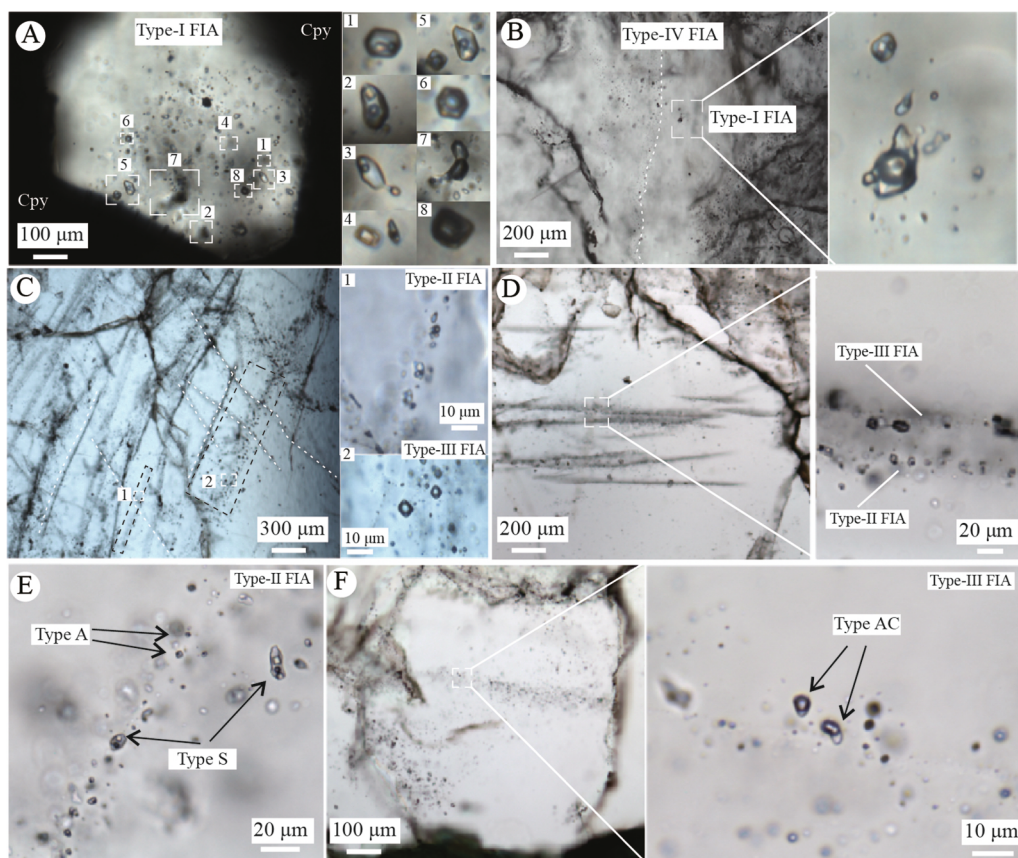


Fig. 6. Photomicrographs of fluid inclusion assemblages from copper-bearing quartz veins, in the Tongwa orebody, from the Henglingguan deposit, Zhongtiao Mountains district. (A) The type-I FIA, consisting of a mixture of halite-bearing inclusions, aqueous-carbonic inclusions and halite-bearing carbonic inclusions, occurs in a clean quartz grain enclosed within the massive chalcopyrite. The left insets (1–7) show the different types of inclusions from this FIA, including halite-bearing inclusions (1–4), aqueous-carbonic inclusions (5–8) and halite-bearing aqueous-carbonic inclusion (6). (B) The type-I FIA next to a healed trail in the quartz vein. (C) The cross cutting of different types of FIAs. Type-II and type-III FIAs occur in the planar arrays and bot cut through by the type-IV FIA. The left insets show the details of type-II FIA (1) and type-III (2). (D) Parallel distributed trails of FIAs within a single quartz grain. The left magnified photograph shows type-II and type-III FIAs in the disparate trails within a single quartz grain. (E) The calcite-halite-bearing inclusion occasionally occurring in type-II FIA. (F) The type-III FIA containing aqueous-carbonic fluids (type AC).

The type-III FIA, consisting of aqueous-carbonic inclusions (type AC), is generally distributed along planar arrays (Fig. 6c) or the healed trails (Fig. 6d) within a single quartz grain. These inclusions are in dark and commonly in rounded or negative crystal shapes, with sizes of 5–12 μm in diameter, consisting of a carbonic phase and an aqueous phase (Fig. 6f). The liquid-like carbonic phase was confirmed to be pure CO_2 by laser Raman spectroscopic analyses (Fig. 8a). The aqueous phase occupies 5–10 vol%. Most of the type AC inclusions were frozen at -90 to -110 $^{\circ}\text{C}$. On heating runs, the final melting temperatures are in the range of -60 to -56.6 $^{\circ}\text{C}$, close to the triple point temperature of pure CO_2 (-56.6 $^{\circ}\text{C}$). Some minor CH_4 may be present in the carbonic phase. With continued heating, these fluid inclusions partially homogenize into the liquid carbonic phase at the temperature of -3.4 to -9.3 $^{\circ}\text{C}$ and totally homogenize into the liquid carbonic phase at the temperatures of 320 to 340 $^{\circ}\text{C}$ (Fig. 9a). The clathrate melting temperature measurements could not be measured with certainty. Thus, the type AC inclusions are simplified as CO_2 - H_2O systems and the $X(\text{CO}_2)$ was calculated to be 56 to 78 mol.% using the FLUID software package of Bakker (2003).

The type-IV FIA, consisting of consistent phase ratios of aqueous inclusions (type A), are commonly distributed in the secondary trails that cut through the whole quartz grains or other types of FIA (Fig. 6c). They possess negative crystal shapes with sizes of 5–15 μm , consisting of a liquid and a vapor phase with the vapor percentages from 10 to 15%. The homogenization temperature of type A inclusions ranges from 90 to 230 $^{\circ}\text{C}$. These inclusions first melted at -23 to -21 $^{\circ}\text{C}$, the final ice melting temperature range from -1.8 to -8.2 $^{\circ}\text{C}$, corresponding to salinities of 4 to 10 wt% NaCl equiv.

4.4. Compositions of individual fluid inclusion

The coexistence of type AC and type S individual inclusions from the copper-bearing hydrothermal veins were selected from LA-ICP-MS

analysis. These two types of fluid inclusions show distinct compositions (Table 3, Figs. 10a–b and 11a–b). The cations of type AC inclusions are dominated by Na (0.69 to 2.3 wt%) and K (0.34 to 1.6 wt%). Type AC inclusions have moderate concentrations of Mg (<443 to 6128 ppm) and Al (<466 to 1494 ppm), and trace concentrations of B (102 to 1930 ppm), Rb (14 to 100 ppm), Sr (4 to 188 ppm), Ba (35 to 318 ppm) and Pb (9 to 822 ppm). Some of the type AC inclusions have detectable ore-forming compositions of Cu (67 to 381 ppm, $n = 2$) and Zn (106 to 629, $n = 4$). The concentrations of Fe, Co, Ni, Ca, and Mn are generally below detection limits. Relative to type AC inclusions (Fig. 11b), type S inclusions have high concentrations of Na (10.9 to 14.7 wt%), Fe (0.47 to 15.7 wt%), K (0.34 to 3.91 wt%), Mg (0.15 to 3.4 wt%) and Mn (0.10 to 2.5 wt%). Type S inclusions contains some detectable ore-forming elements of Cu (113 to 3004 ppm, $n = 7$), Zn (256 to 3256 ppm, $n = 27$), Co (3 to 17 ppm, $n = 5$) and Ni (122 to 179 ppm, $n = 2$). Type S inclusions have trace concentrations of B (111 to 1057 ppm), Rb (8 to 356 ppm), Sr (63 to 3752 ppm), Ba (89 to 2227 ppm), and Pb (73 to 2029 ppm).

5. Discussion

5.1. Evidence for fluid immiscibility in the H_2O -NaCl- CO_2 system

Based on the fluid inclusion petrography, microthermometry results, and laser Raman analyses, it is suggested that the ore fluids at the Henglingguan deposit most likely had a complex fluid composition of NaCl - CaCO_3 - H_2O - CO_2 . Thus, the relationship between type-I, type-II, and type-III FIAs in these sulfide-bearing quartz veins is the key to understand the ore fluid evolution during sulfide mineralization and quartz vein formation.

The type-I FIA has a mixture of type AC and type S inclusions (Fig. 6a–b). Some of the type AC inclusions even occasionally captured tiny cubic halite solid (Fig. 6a–b), further indicating heterogenous


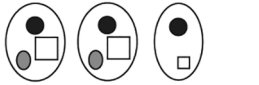

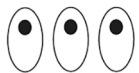
<p>Type-I FIA (Primary)</p> 	<p>Coexisting halite-bearing and liquid carbonic phase-bearing inclusions in the planar arrays of quartz core. Provide evidence of fluid immiscibility.</p>
<p>Type-II FIA (Pseudo-secondary?)</p> 	<p>High-salinity aqueous inclusions occurring in the planar arrays or the healed trails. Provide information of the dense saline fluid after fluid immiscibility.</p>
<p>Type-III FIA (Pseudo-secondary?)</p> 	<p>CO₂-rich carbonic inclusions occurring in the planar arrays or the healed trails. Provide information of the less dense CO₂-rich phase after fluid immiscibility.</p>
<p>Type-IV FIA (Secondary)</p> 	<p>Low-temperature, low-salinity aqueous inclusions that crosscut quartz grains and other generations of FIAs.</p>

Fig. 7. Schematic illustration of four types FIA identified in this study, along with a summary of information available from each types of FIA.

entrapment. The type-II and type-III FIAs occurred in quartz grains separately or coexisted within a single quartz grain. The distribution and composition of type-II and type-III FIA revealed that a carbonic fluid phase was trapped during quartz vein formation or in the heal fractures. Microthermometric results show that most of the halite crystals in the type-II FIA have a variable melting temperature of 210 to 350 °C and some halite did not dissolve at the same temperature. The variable of halite melting temperature may be caused by the necking down through a phase transition boundary. In this case, we may overestimate its salinity. Considering that not all fluid inclusions from the type-II FIA contain calcite, it is likely to be accidentally entrapped solid (e.g., Chi et al., 2021). Microthermometric results show that type AC inclusions

from the type-III FIA have a narrow range of homogenization temperatures (320 to 340 °C). The wide range of estimated X(CO₂) values of 56 to 78 mol.% is probably due to the imprecise visual estimation of carbonic/aqueous phase proportions.

The heterogeneous fluid entrapment in the type-I FIA could be the result of by fluid–fluid immiscibility. The type-II and type-III FIA are likely to be the separated end-member fluids after the fluid immiscibility. If the fluid immiscibility occurred, the coexisting fluid inclusions should be compatible with fluid phase equilibria (Pichavant et al., 1982; Ramboz et al., 1982; Chi et al., 2021). Based on the above analytical results, the ore fluid can be simplified as H₂O-NaCl-CO₂ system, which could experience fluid–fluid immiscibility over the whole range of metamorphic conditions (e.g., Heinrich, 2007). When fluid immiscibility occurs, a homogenous parent fluid separates a dense and saline phase, and a less dense and CO₂-rich phase, sometimes even some supersaturated crystal salts (Heinrich, 2007; Yardley and Bodnar, 2014). Fluid inclusions formed from such phase separation fields could conceivably trap a mechanical mixture of distinct phases. We plotted the fluid compositions obtained from these different types of FIAs in the phase diagram of the H₂O-NaCl-CO₂ fluid system at 350 °C and 3.5 kbar (Fig. 13a). The type-I FIA corresponds to the mechanical mixture of distinct fluid phases; the type-II FIA might refer to saline end member; and the type-III FIA refers to the CO₂-rich end member. The homogenization temperature (320 to 340 °C) in type-III FIA is suggested to be close to the fluid inclusions trapping conditions. According to isochores of type AC inclusions in the type-III FIA, the trapping pressure is constrained at 3.5 to 4.0 kbar. One of the key phase diagram analyses to support the possibility of fluid immiscibility is that the saline and CO₂-rich parent fluid can exist in the one-phase field (i.e., before immiscibility) at the elevated P-T condition. The fluid phase diagram of H₂O-NaCl-CO₂ system at 450 °C and 4.5 kbar is also shown in Fig. 13a. The composition of parent fluid is likely constrained in the yellow zone marked in Fig. 13a. At this zone, the parent fluid would be a homogeneous aqueous fluid with X(NaCl) of 10 to 20 mol.% (approximal to the salinity of 23 to 41 wt%) and X(CO₂) of 10 to 15 mol.%. Upon fluid cooling and decompression, this homogenous CO₂-rich brine fluid would split into a CO₂-poor brine fluid and CO₂-rich carbonic fluid. As discussed above, the type-II FIA could be inferred as the endmember of CO₂-poor brine fluid and the type-III FIA represents the endmember of CO₂-rich carbonic fluid. Nevertheless, it should be in caution that most inclusions in these FIAs are likely to be subjected to post-entrapment modification (e.g., necking down through a phase transition boundary).

The heterogeneously fluid trapping could also be interpreted as fluids mixing. The mixing of fluids of different compositions may also be applied to interpret these different types of FIAs trapped almost at the same time. However, the fluid mixing model cannot interpret the separate distribution of the type-II and type-III FIAs in the healed

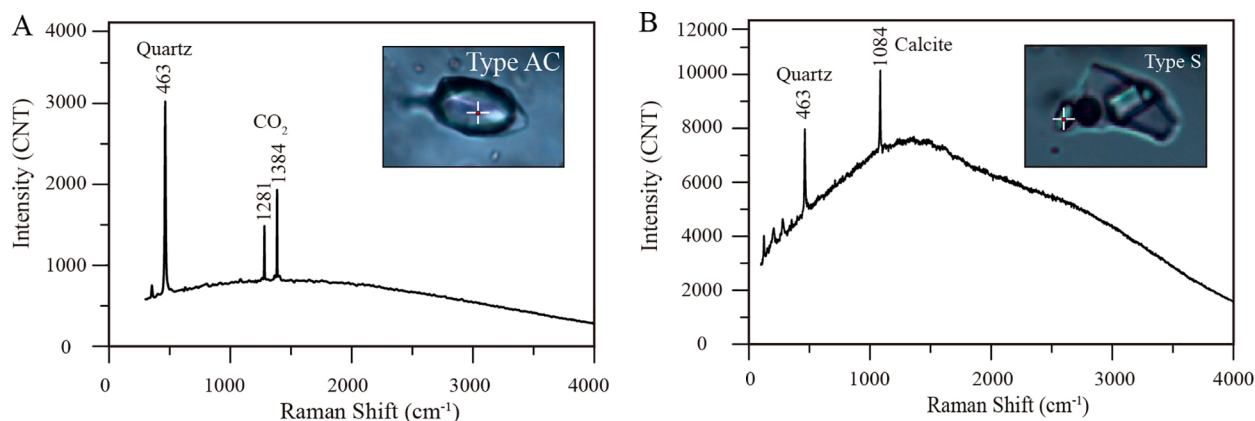


Fig. 8. Laser Raman analyses of representative inclusion types. (A) Carbonic phase in type AC inclusions was analyzed with laser Raman spectroscopy showing CO₂ peak, but no CH₄, N₂, or H₂S peaks. (B) Round solid grains in type S inclusions were analyzed with laser Raman spectroscopy showing typical calcite peak.

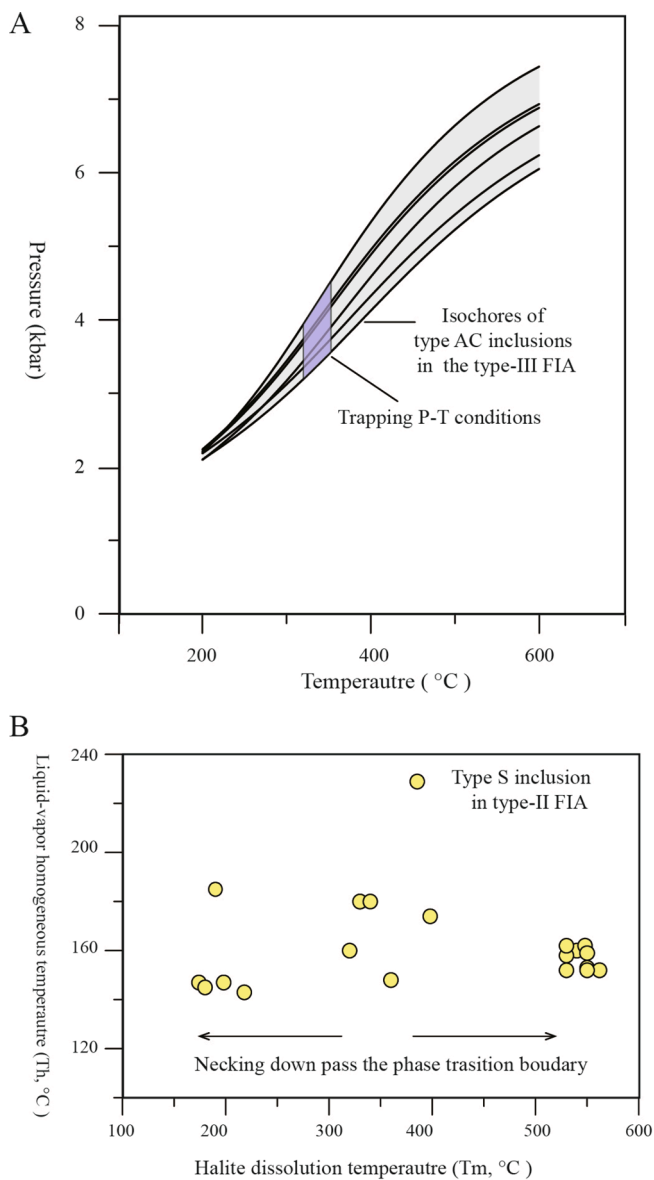


Fig. 9. Microthermometric results. (A) The homogenous pressure condition inferred from the isochores of type AC in the type-III FIA based on their homogenization temperature. (B) Liquid-vapor homogenization temperature (T_h) - halite dissolution temperature (T_m) of type S inclusions in the type-II FIA.

fractures in quartz grains (Fig. 6b). Moreover, these two fluids have distinct physicochemical properties. For example, the different wetting dihedral angles of these two fluids could result of separately fluid migration. Thus, they hardly could mix as a single fluid phase.

All the fluid inclusions were selected from the late stage of vein-type mineralization (M-2), which is dominated by chalcopyrite-pyrrhotite-arsenopyrite-pyrite assemblage in the quartz veinlets. A previous study on sphalerite geothermobarometer results in quartz veins revealed the sulfide precipitation condition at the temperature of ~ 350 °C and pressure of ~ 3.5 kbar (Qiu et al., 2017). The previous study on the arsenopyrite-bearing sulfide assemblages in the quartz veinlets shows a relatively high temperature of 420 to 480 °C. The data indicate fluid cooling from the veinlet mineralization to quartz vein mineralization. Based on the fluid phase analysis (Fig. 13a), the decrease of fluid temperature from 450 °C to 350 °C and fluid pressure could make a CO_2 -bearing brine fluid unstable. It would separate into a CO_2 -rich fluid phase and a brine fluid phase. Thus, fluid cooling and decompression are likely to be the main triggers for the fluid–fluid immiscibility. The decrease

of fluid pressure could also promote phase separation

5.2. Metamorphic source for the saline ore fluid

The high-temperature NaCl-rich fluid is commonly an indication of magmatic origins that it is released from felsic magmas (e.g., Ridley and Diamond, 2000; Sillitoe, 2010). However, the geological setting and sulfur isotope characteristics do not support the magmatic origins model. The hydrothermal monazites from Cu-bearing veinlets revealed that the Cu mineralization occurred at ~ 1860 Ma (Qiu et al., 2017), close to the metamorphic age of ~ 1890 Ma estimated from metamorphic monazites in the host metasedimentary rocks (Qiu et al., 2017). No contemporary magmatic activity was reported in the Henglingguan Cu deposit. The intercalated amphibolite was considered to have intruded during 2160–2190 Ma based on U-Pb isotopic dating on zircons (Liu et al., 2015). Moreover, the sulfides in the Cu-bearing veinlets and veins have negative sulfur isotope signatures of -10 to -11 ‰ (Fig. 3a–c), which strongly support a sedimentary source of sulfur. Thus, the magmatic source of ore-forming fluid is excluded for the formation of the Henglingguan Cu deposit.

In comparison with the major parameters of other hydrothermal deposits (Fig. 13b), the copper deposit in this study shows fluids with high salinity ($X_{\text{NaCl}} = 0.1$ to 0.2) and significant CO_2 contents ($X_{\text{CO}_2} = 0.1$ to 0.15). The combination of high salinity and high CO_2 contents makes the ore fluid distinct from almost of the other major hydrothermal deposits. The ore fluids of most porphyry deposits are hyposaline aqueous fluid (magmatic brine) and weakly saline aqueous vapors (e.g., Sillitoe, 2010; Heinrich and Candela, 2014). For high- and low-sulfidation epithermal deposits, the ore fluids are dominantly in low salinity aqueous fluid with trace CO_2 (e.g., Hedenquist and Lowenstern, 1994). The ore fluids in the orogenic gold deposits are consistent with low salinity and are CO_2 rich (e.g., Goldfarb et al., 2005). This unique ore fluid in the Henglingguan Cu deposit is therefore not derived from felsic magmas or metamorphic dehydration of common pelitic rocks.

The ore fluid at the Henglingguan Cu deposit has a composition distinct with magmatic brine and basinal brine (Fig. 12a–b). In the Na-Ca-K ternary plot, the ore fluid is richer in Na and Ca contents than those of the magmatic brine from typical porphyry to epithermal Cu-Cu-Au-Mo deposits worldwide (Fig. 12a). In the Ba-Rb-Sr trace elements ternary plot (Fig. 12b), the ore fluid in this studied area is closing to the basinal brine but distinct from the magmatic brine. These two features suggest that the ore fluid composition is located between these two endmembers and evolved towards Sr-Ba enrichment. Sedimentary basin fluids are enriched in trace elements Sr and Ba (Fig. 12b, Large et al., 2016), whereas the magmatic brine is generally enriched in Rb and depleted in Ba (Fig. 12b, Williams-Jones et al., 2010). Thus, it is indicated that the ore fluid in this Cu deposit involved the reaction with sedimentary host rocks during its generation.

The generation of high temperature, high salinity, and high CO_2 fluid requires that ore fluid can infiltrate rocks in deep crust during orogenesis. Because the ore fluids are rich in both NaCl and CO_2 , they could only be stable at high crustal P-T conditions based on the phase diagram of the H_2O -NaCl- CO_2 fluid system (Fig. 13a). Once cooling or decompression occurs, this homogenous ore fluid would easily separate into the brine fluid phase and carbonic fluid phase as discussed above. Metamorphism and magmatism are the main sources of such fluids. The magmatic source is excluded based on the above discussions regarding the geological setting, geochronology, sulfur isotopes, and fluid compositions. The metamorphic dehydration of common pelitic rocks and mafic rocks would release low salinity and CO_2 -rich metamorphic fluid, not metamorphic brine (e.g., Phillips and Powell, 2010). In the Zhongtiao area, the orogenic belt contains evaporative siliceous limestone and carbonate-bearing argillites rocks (Qiu et al., 2021a). These evaporative rocks could be a candidate source to release high salinity and CO_2 -rich metamorphic brine. They could provide the source of NaCl and CO_2 during the metamorphic dehydration and decarbonation under high-

Table 3
In-situ LA-ICP-MS chemical composition analyses result for individual fluid inclusions from copper-bearing quartz veins in the Henglingguan Cu deposit.

Analysis	Na	K	Ca	Fe	Mn	Mg	Al	Co	Ni	Cu	Zn	B	Rb	Sr	Ba	Pb
	(ppm)	(ppm)	(ppm)	(ppm)	(ppm)	(ppm)	(ppm)	(ppm)	(ppm)	(ppm)	(ppm)	(ppm)	(ppm)	(ppm)	(ppm)	(ppm)
NO.																
Type AC inclusions*																
A43	13,379	3435	<10323	<2237	<129	<443	365	<14	<241	<98	<25	<427	18	128	39	20
A44	22,969	14,669	<18885	<4557	<237	1019	3733	<46	<536	<243	<91	<666	40	188	318	124
A51	170,545	10,243	<50711	<13391	1629	<2263	<466	<90	<1151	<619	629	<1930	100	34	76	822
A56	17,204	15,620	<13556	<3857	<189	984	869	<35	<305	381	493	<791	14	13	229	23
A74	22,108	8635	<31040	<7759	<396	3265	1494	<55	<788	<327	536	<274	68	31	44	133
A75	7230	7318	<24229	<5938	<295	6128	1210	<47	<662	<331	<348	<633	65	13	35	41
A57	6891	3757	25,802	<834	<38	2037	752	<5	<73	67	106	<102	15	4	115	9
Average	37,189	9097	25,802	–	1629	2687	1404	–	–	224	441	–	46	59	122	167
1 SD	59,154	4811	–	–	–	2138	1205	–	–	222	230	–	33	71	110	293
Type D inclusions**																
A46	135,536	39,100	<5087	17,146	8946	3248	395	<8	<142	113	3256	<186	85	117	1563	746
A49	136,723	31,170	<10768	10,918	5999	13,132	776	<20	<322	3004	2394	422	113	338	309	425
A60	146,826	3386	<16432	29,688	10,397	1470	<169	<28	<469	328	757	465	32	63	367	73
A62	108,519	7252	<24909	74,391	17,189	<1186	<219	<32	<709	<305	716	824	63	97	89	243
A63	115,820	11,907	<10676	51,674	5945	<408	352	<4	<303	<112	1047	523	163	262	495	241
A69	121,998	7084	<12632	56,375	6878	<518	<118	5	<300	<167	750	260	82	266	672	986
A71	144,603	5326	<3657	33,198	3500	<158	62	<7	<98	<52	256	111	47	127	292	697
A50	95,908	29,965	21,731	44,416	13,123	<171	315	<5	<103	<54	2742	612	160	133	217	679
A48	106,357	15,080	21,253	42,754	17,906	2644	2312	6	<106	<63	2850	144	202	377	1093	256
A52	19,126	14,045	16,146	156,912	4854	15,734	3536	<12	179	134	2596	312	71	124	1874	308
A59	35,444	31,777	20,108	119,518	25,447	9211	894	<5	<244	311	1768	349	68	150	401	267
A64	87,008	24,631	41,191	32,772	3512	1872	<105	16	<269	<107	1062	394	293	992	953	131
A70	95,653	18,999	48,742	12,266	6269	<578	264	<24	<335	<151	3156	492	356	3752	2227	2029
A72	95,686	21,059	39,779	25,752	5176	1916	486	<38	<899	<393	1750	648	104	1626	859	617
A73	132,474	16,103	12,397	24,182	3739	3674	<77	17	<222	<97	1013	332	171	451	912	672
A76	24,955	37,386	106,227	8465	1049	33,709	12,855	<41	<719	810	1250	1057	54	162	332	482
A61	10,857	6500	137,548	4693	6848	1939	752	3	122	249	590	143	8	352	99	198
Average	94,911	18,869	46,512	43,831	8634	8050	1917	9	151	707	1644	443	122	552	750	532
1 SD	45,252	11,659	42,121	40,615	6381	9861	3589	7	40	1039	993	254	93	914	631	463

* Concentrations quantification for type AC inclusions are constrained by 10 equiv. wt.% NaCl (charge balance).

** Concentrations quantification for type D inclusions are constrained by 45 equiv. wt.% NaCl (charge balance).

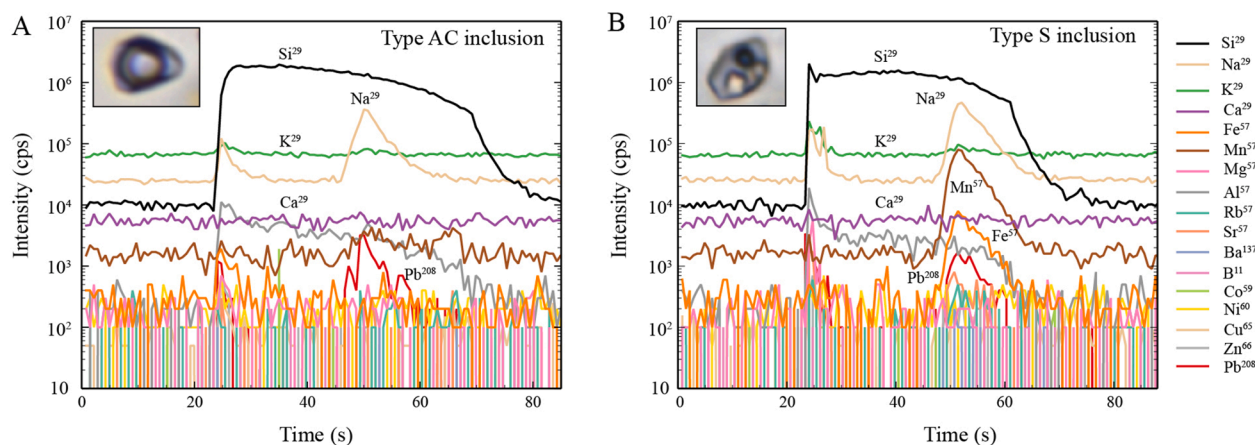


Fig. 10. Representative LA-ICP-MS signals of different fluid inclusion types at Henglingguan. (A) The aqueous-carbonic inclusion (type AC). (B) The solid mineral-bearing inclusion (type S). The petrography of corresponding fluid inclusions is shown in the upper-left inset of each panel.

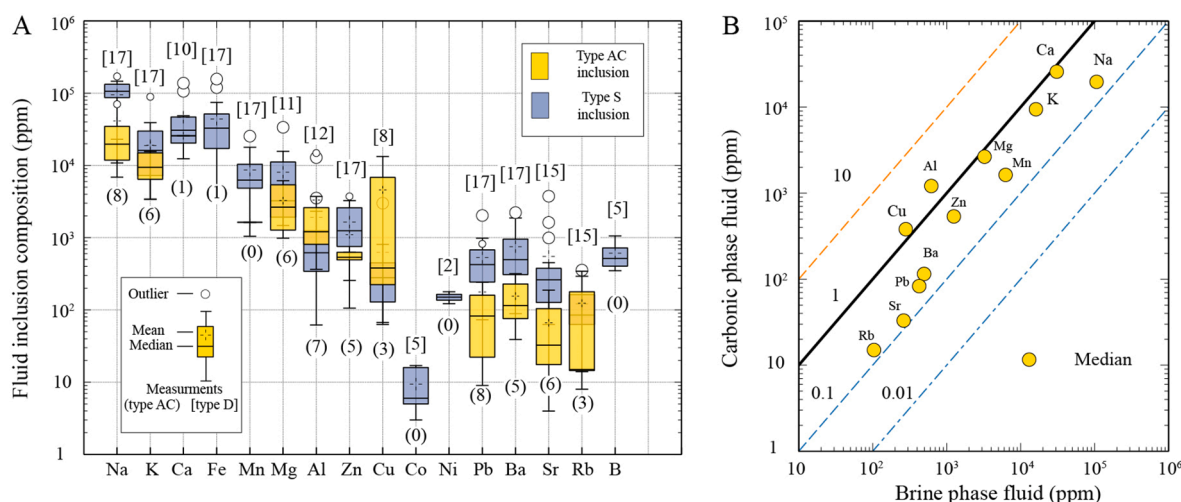


Fig. 11. LA-ICP-MS results for individual fluid inclusions. (A) Box plot of element concentrations in carbonic (type AC) and brine inclusions (type S) from Henglingguan. The bar = median; box = 25 to 75 percentiles of data; small open circles = outliers of type AC inclusions; large open circles = outliers of type S inclusions; whiskers = 1.5 times of the length of the box toward the maximum and minimum. The numbers in brackets and square brackets are the total measurements of each element for the type AC and type S inclusions, respectively. (B) The correlation between median element concentrations in carbonic and brine inclusions.

grade metamorphism. Such a deep metamorphic brine fluid would drive the base-metal transportation and mineralization (cf. Morrissey and Tomkins, 2020; Qiu et al., 2021a).

5.3. Implications for saline metamorphic hydrothermal ore formation

The Zhongtiao Mountains are located in the southern section of TNCO. The tectonic evolution of TNCO, especially from 2200 to 1800 Ma, has been debated for a long time. Some mutually exclusive models have been proposed to interpret the central part of the NCC (Trap et al., 2007; Santosh, 2010; Kusky, 2011; Zhao and Zhai, 2013; Zhai and Santosh, 2013; Peng et al., 2014; Tang and Santosh, 2018). Combining with the metamorphic P-T-t-m evolution path of the Henglingguan deposit proposed by Qiu et al. (2017) and a comprehensive understanding of the ore fluids evolution in this area, a saline metamorphic hydrothermal ore formation is proposed to explain the epigenetic hydrothermal Cu deposits hosted in the metasedimentary rocks (Fig. 14). The source-transportation-precipitation of metallic elements was likely linked to the formation and closure of the Zhongtiao rift during ~ 2.2 to 1.85 Ga (Fig. 14).

The first stage started with the open phase of an intra-continental rift

or back-arc basin that formed in the Archean shield (Fig. 14a). The basement rocks comprise voluminous ~ 2.7 to 2.5 Ga tonalite-trondhjemite-granodiorite and ~ 2.3 Ga Paleoproterozoic granitoids. The sedimentary-volcanic rock sequences were deposited in the rift basin at ~ 2.2 to ~ 2.1 Ga. This rift basin contains bimodal volcanic rocks, immature clastic sediments, sulfidic carbonaceous shales, and evaporitic carbonate rocks. These rocks have the potential to provide metal sources for epigenetic hydrothermal mineralization. For example, the recent study on the *in-situ* pyrite Fe-S isotopes and trace element compositions shows that the sulfidic carbonaceous shales are good Cu-Co source rocks (Qiu et al., 2016; Qiu et al., 2021b). In the Henglingguan Formation of Jiangxian Group, some Co-Fe-Ni sulfide (cobaltite) grains occurring as inclusions within garnet also supported the metallic elements pre-enrichment in the protolith of mica-schist (Qiu et al., 2017). The precursor rocks of mica-schist are speculated to originally enrich in Cu-Co metallic elements. Although this study lacks effective isotopic tracers for metal sources, the negative sulfur isotope signatures of -10 to -11 ‰ obtained from the hydrothermal sulfides in quartz veins suggest that the sulfur was derived from a source rock of sedimentary origin.

The second stage is referred to as the rift closure, basin inversion, and

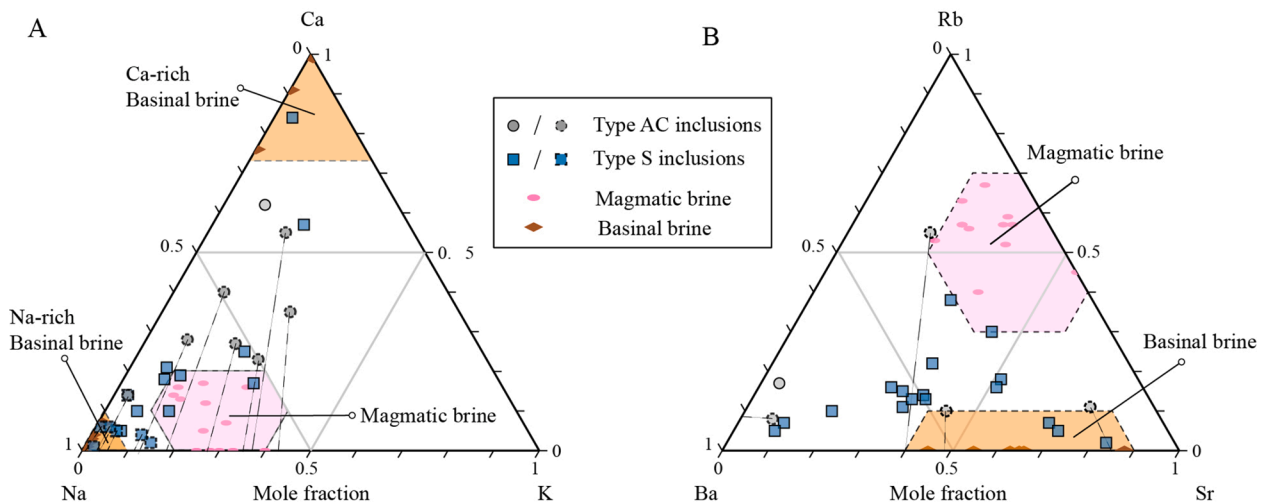


Fig. 12. Comparison of fluid chemistry from this *meta-sedimentary* hosted Cu deposit at Henglingguan with the endmember fluid fields of magmatic brine and basinal brine. (A) Mole fraction plot of Ca-Na-K diagram; (B) Mole fraction plot of Rb-Ba-Sr diagram. The magmatic brine field is constrained by the data points in pink hexagon from Butte, porphyry Cu-Mo deposit, Montana, USA (Rusk et al., 2004), Bingham Canyon, porphyry Cu-Mo-Au deposit, Utah, USA (Large et al., 2016) and Rongna, porphyry-epithermal Cu-(Au) deposits, Tibet, China (Zhang et al., 2020). The basinal brine field is constrained by the data points in brown hexagon from halite rock and anhydrite rock evaporite, Grand County, Utah, USA (Kharaka and Hanor, 2014).

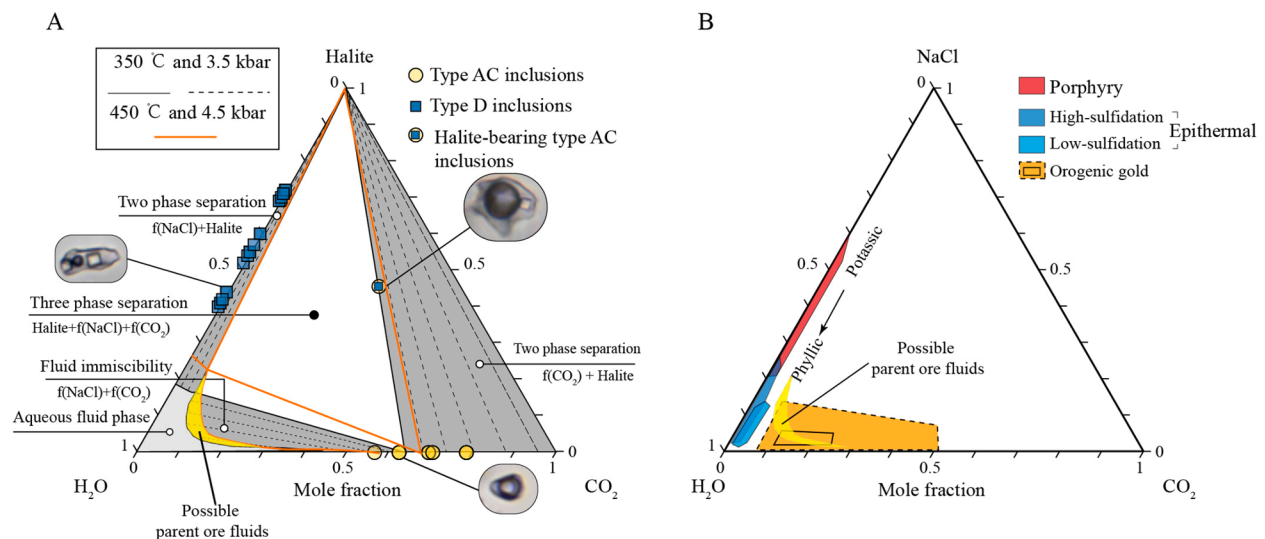
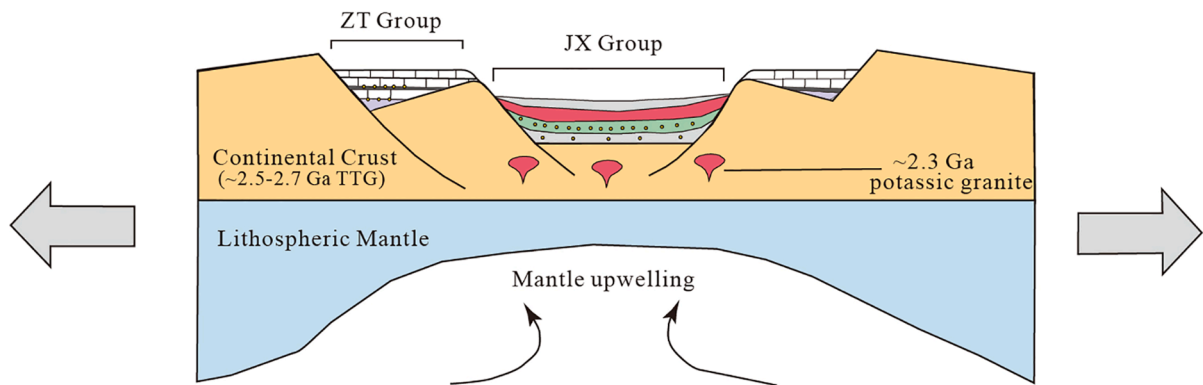


Fig. 13. H₂O-NaCl-CO₂ system of ore fluids. (A) The phase diagrams of the H₂O-CO₂-NaCl ternary system are calculated using the software package of Perple X 6.6.8 at 350 °C, 3.5 kbar and 450 °C, 4.5 kbar, respectively (Connolly, 2005). The triangle white area refers to a three-phase separation field. The fluid composition in the field would split into a brine fluid, a carbonic fluid, and halite solid, as the brown arrows are shown. Occasionally, brine fluid and carbonic fluid would capture halite solids, such that their compositions would evolve along with the blue and yellow arrows. Grey areas refer to two-phase separation fields. The light grey area refers to a single phase of aqueous fluid. These $f(\text{NaCl})$ and $f(\text{CO}_2)$ phases represent high salinity aqueous phase and CO₂-rich carbonic fluid, respectively. (B) Composition of ore fluid at the Henglingguan Cu deposit in comparison with different types of hydrothermal deposits with respect to molar proportions of H₂O, CO₂, and salinity (equiv. wt.% NaCl, expressed as a molar proportion). The fields of porphyry, epithermal and orogenic gold deposit are taken from Ridley and Diamond (2000).

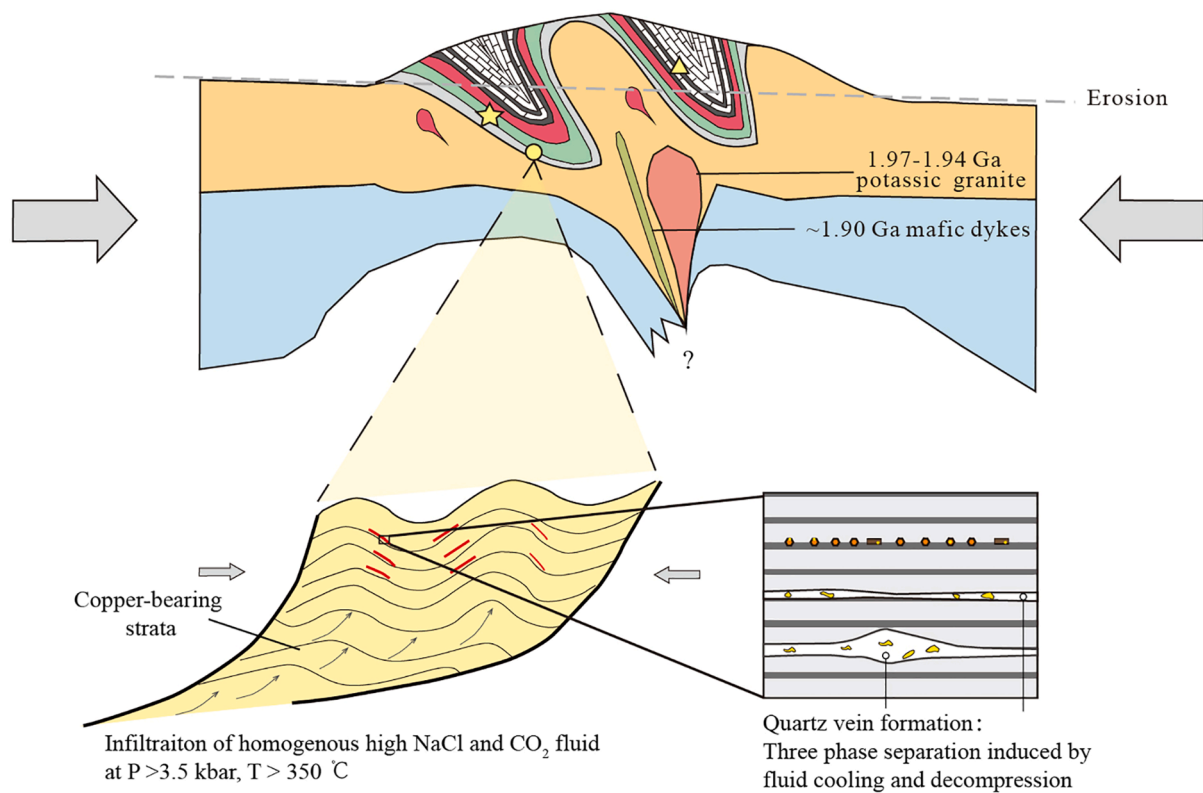
the subsequent post-collision exhumation (Fig. 14b, ~1.95 to ~1.85 Ga). As the rift basin closed, the continental crust was thickening, as evidenced from the potassic granitoids in the Sushui Complex southern of the Zhongtiao Mountains. Geochemistry and petrogenetic study on the potassic granitoids indicated that they were derived from partial melting of Archean TTG rocks in an over thickened continental crust (Tian et al., 2006). Zircon SHRIMP U-Pb dating revealed that these potassic granitoids were emplaced during ~1968 to ~1944 Ma, and is interpreted to mark the timing of the collision. During this collision process, the host cupriferous sedimentary rocks in the Henglingguan Formation were subjected to lower amphibole facies metamorphism under the P-T conditions of 6.4 to 6.5 kbar and 615 to 630 °C, as revealed by the mineral geothermobarometry and phase diagram

computations of the mica-schist and amphibolite (Qiu et al., 2017). The mechanism of Cu and Co metallic elements liberation or remobilization from the cupriferous source rocks is not quite clear. Nevertheless, the metamorphic brine is suggested to have played a key role in the liberation and transportation of Cu-Co into the metamorphic fluid. The basis for this suggestion is the understanding that the solubility of base metals is strongly enhanced in the Cl-rich hydrothermal fluids (Yardley, 2005; Seward et al., 2014; Yardley and Cleverley, 2015; Brugger et al., 2016). The source rocks for essentially H₂O, NaCl, and CO₂ could be evaporitic carbonate rocks and/or carbonate-bearing argillites. Previous geochronology study constrained the Henglingguan Cu mineralization age at ~1867 Ma from the U-Th-Pb dating of hydrothermal monazite. It is suggested that fertile saline metamorphic hydrothermal fluids deposited

A Rift open phase and passive continent margin setting (~2.2-2.0 Ga):



B Rift closure and basin inversion (1.95-1.85 Ga):



Jiangxian Group (JX) (~2.2 to ~2.1 Ga)		Zhongtiao Group (ZT) (~2.1 Ga to ~2.0 Ga)		Epigenetic hydrothermal Cu deposit (~1.9 Ga to ~1.85 Ga)	
LEGEND	Acid volcanic rocks	Dolostone &imestone	Tongkuangyu Cu deposit in the JX Group	Mental sources	
	Basic volcanic rocks	Organic shales	Henglingguan Cu deposit in the JX Group	Sulfides assemblage	
	Clastic rocks	Clastic rocks	Bu-Bi type Cu deposit in the ZT Group	Metamorphic minerals	

Fig. 14. Schematic cartoon model depicting the formation of the Henglingguan epigenetic hydrothermal Cu deposit from the rift open phase (A) to rift closure phase and basin inversion (B) in the Zhongtiao Mountains district.

hydrothermal sulfides during the retrograde cooling. The fluid cooling and decompression are likely the main triggers for the phase separation and the final Cu-(Co) mineralization in quartz veins.

6. Conclusions

The Henglingguan Cu-(Co) deposit in the Zhongtiao Mountains district is an epigenetic hydrothermal Cu deposit hosted within the *meta*-sedimentary rocks, consisting of early disseminated mineralization and quartz vein mineralization. A model of saline metamorphic hydrothermal mineralization at the retrograde stage is proposed to interpret the ore genesis.

- (1) The parent ore fluid was likely subjected to the fluid immiscibility based as inferred from fluid inclusion petrography observations, microthermometry results, and fluid phase analysis of the H₂O–NaCl–CO₂ system. The fluid immiscibility P–T condition is constrained at 320 to 340 °C and 3.5 to 4.0 kbar according to the homogenization temperature–pressure conditions for the end-member of carbonic fluid inclusion.
- (2) The combination of high salinity and high CO₂ contents makes the ore fluid in the Henglingguan Cu deposits distinct from almost of the other major hydrothermal deposits. The parent ore fluid before fluid immiscibility had high salinity ($X_{\text{NaCl}} = 0.1$ to 0.2) and significant CO₂ contents ($X_{\text{CO}_2} = 0.1$ to 0.15) based on the fluid phase analysis. *In-situ* composition analysis of individual fluid inclusions by LA-ICP-MS show that the ore fluid is rich in Na, Ca, Fe and Mn, and evolved towards Sr–Ba enrichment in the Ba–Rb–Sr ternary plot. This indicates that the ore fluid is metamorphic brine derived from the evaporitic sedimentary rocks. The negative sulfur isotope data (–10 to –11 ‰) further suggests a sedimentary rock source of sulfur for the hydrothermal Cu mineralization.
- (3) The high salinity and high CO₂ fluids are likely derived from the evaporative carbonate rocks developed on the basin margins or passive continental margins. This metamorphic brine served as effective medium in the transportation of Cu along its flow paths. The fluid cooling and decompression during the retrograde stage/post-collision exhumation were the key triggers for fluid immiscibility. The fluid unmixing is likely responsible for Cu mineralization in the quartz veins.

Declaration of Competing Interest

The authors declare that they have no known competing financial interests or personal relationships that could have appeared to influence the work reported in this paper.

Acknowledgments

We are grateful to Drs. Kuidong Zhao, Zhihui Dai, and Yinghua Chen for their kind support with the analytical experiments. Associate Editor Prof. Guoxiang Chi and two anonymous reviewers are thanked for their constructive comments, which improved the quality of this manuscript. This study was supported by the National Nature Science Foundation of China grants 41890833 and 41902080.

Appendix A. Supplementary data

Supplementary data to this article can be found online at <https://doi.org/10.1016/j.oregeorev.2021.104462>.

References

- Allan, M.M., Yardley, B.W., Forbes, L.J., Shmulovich, K.I., Banks, D.A., Shepherd, T.J., 2005. Validation of LA-ICP-MS fluid inclusion analysis with synthetic fluid inclusions. *Am. Mineral.* 90, 1767–1775.
- Bakker, R.J., 2003. Package FLUIDS 1. Computer programs for analysis of fluid inclusion data and for modelling bulk fluid properties. *Chem. Geol.* 194, 3–23.
- Brugger, J., Liu, W., Etschmann, B., Mei, Y., Sherman, D.M., Testemale, D., 2016. A review of the coordination chemistry of hydrothermal systems, or do coordination changes make ore deposits? *Chem. Geol.* 447, 219–253.
- Chi, G., Diamond, L.W., Lu, H., Lai, J., Chu, H., 2021. Common problems and pitfalls in fluid inclusion study: A review and discussion. *Minerals* 11, 7.
- Connolly, J.A.D., 2005. Computation of phase equilibria by linear programming: a tool for geodynamic modeling and its application to subduction zone decarbonation. *Earth Planet. Sci. Lett.* 236, 524–541.
- Diamond, L.W., 2001. Review of the systematics of CO₂–H₂O fluid inclusions. *Lithos* 55, 69–99.
- Eglinger, A., Vanderhaeghe, O., André-Mayer, A.S., Goncalves, P., Zeh, A., Durand, C., Delouie, E., 2016. Tectono-metamorphic evolution of the internal zone of the Pan-African Lufilian orogenic belt (Zambia): Implications for crustal reworking and syn-orogenic uranium mineralizations. *Lithos* 240, 167–188.
- Fan, H.R., Zhai, M.G., Xie, Y.H., Yang, J.H., 2003. Ore-forming fluids associated with granite-hosted gold mineralization at the Sanshandao deposit, Jiaodong gold province, China. *Miner. Deposita* 38, 739–750.
- Goldfarb, R., Baker, T., Dubé, B., Groves, D. I., Hart, C. J., Gosselin, P., 2005. Distribution, character and genesis of gold deposits in metamorphic terranes. In: Hedenquist, J.W., Thompson, J.F.H., Goldfarb, R.G., Richards, J.P. (Eds.), *Economic Geology 100th Anniversary Volume*. Society of Economic Geologists, Littleton, Colorado, USA, pp. 407–450.
- Goldstein, R.H., Reynolds, T.J., 1994. Fluid Inclusion Petrography. In: Goldstein, R.H., Reynolds, T.J. (Eds.), *Systematics of Fluid Inclusions in Diagenetic Minerals (SEPM Short Courses 31)*. SEPM (Society for Sedimentary Geology), Tulsa, OK, USA, pp. 69–85. <https://doi.org/10.2110/scn.94.31.0069>.
- Goldstein, R.H., 2001. Fluid inclusions in sedimentary and diagenetic systems. *Lithos* 55, 159–193.
- Gregory, M.J., Schaefer, B.F., Keays, R.R., Wilde, A.R., 2008. Rhenium–osmium systematics of the Mount Isa copper orebody and the Eastern Creek Volcanics, Queensland, Australia: implications for ore genesis. *Miner. Deposita* 43, 553.
- Groves, D.I., Goldfarb, R.J., Robert, F., Hart, C.J., 2003. Gold deposits in metamorphic belts: overview of current understanding, outstanding problems, future research, and exploration significance. *Econ. Geol.* 98, 1–29.
- Groves, D.I., Bierlein, F.P., 2007. Geodynamic settings of mineral deposit systems. *J. Geol. Soc. London* 164, 19–30.
- Guillong, M., Meier, D.L., Allan, M.M., Heinrich, C.A., Yardley, B.W., 2008. Appendix A6: SILL: A MATLAB-based program for the reduction of laser ablation ICP-MS data of homogeneous materials and inclusions. *Mineral. Assoc. Canada Short Course* 40, 328–333.
- Hammerli, J., Rubenach, M., 2018. The Role of Halogens During Regional and Contact Metamorphism. In: Harlow, D., Aranovich, L. (Eds.), *The Role of Halogens in Terrestrial and Extraterrestrial Geochemical Processes*. Springer Geochemistry, Springer, Cham, pp. 649–712. https://doi.org/10.1007/978-3-319-61667-4_10.
- Hedenquist, J.W., Lowenstern, J.B., 1994. The role of magmas in the formation of hydrothermal ore deposits. *Nature* 370, 519–527.
- Heinrich, C.A., Candela, P.A., 2014. Fluids and ore formation in the Earth's crust. In: Scott S.D. (Ed.), *Geochemistry of Mineral Deposits*, pp. 1–28. <https://doi.org/10.1016/B978-0-08-095975-7.01101-3>.
- Heinrich, C.A., Pettke, T., Halter, W.E., Aigner-Torres, M., Audétat, A., Günther, D., Hattendorf, B., Bleiner, I., Horn, I., 2003. Quantitative multi-element analysis of minerals, fluid and melt inclusions by laser-ablation inductively-coupled-plasma mass-spectrometry. *Geochim. Cosmochim. Acta* 67, 3473–3497.
- Heinrich, C.A., 2005. The physical and chemical evolution of low-salinity magmatic fluids at the porphyry to epithermal transition: a thermodynamic study. *Miner. Deposita* 39, 864–889.
- Heinrich, W., 2007. Fluid immiscibility in metamorphic rocks. *Rev. Mineral. Geochem.* 65, 389–430.
- Hu, W.X., Sun, D.Z., 1987. Mineralization and evolution of the Early Proterozoic copper deposits in the Zhongtiao Mountains. *Acta Geol. Sin.* 61, 61–76.
- Jiang, Y., Niu, H., Bao, Z., Li, N., Shan, Q., Yang, W., 2014. Fluid evolution of the Tongkuangyu porphyry copper deposit in the Zhongtiao Mountains region: Evidence from fluid inclusions. *Ore Geol. Rev.* 63, 498–509.
- Kharaka, Y.K., Hanor, J.S., 2014. Deep fluids in sedimentary basins. In: Holland, H., Turekian, H.D.H.K. (Eds.), *Treatise on Geochemistry (Second Edition)*: Oxford. Elsevier, UK, pp. 471–515.
- Kusky, T.M., 2011. Geophysical and geological tests of tectonic models of the North China Craton. *Gondwana Res.* 20, 26–35.
- Lan, T.G., Hu, R.Z., Bi, X.W., Mao, G.J., Wen, B.J., Liu, L., Chen, Y.H., 2018. Metasomatized asthenospheric mantle contributing to the generation of Cu–Mo deposits within an intracontinental setting: a case study of the ~128 Ma Wangjiazhuang Cu–Mo deposit, eastern North China Craton. *J. Asian Earth Sci.* 160, 460–489.
- Large, S.J., Bakker, E.Y., Weis, P., Wälle, M., Ressel, M., Heinrich, C.A., 2016. Trace elements in fluid inclusions of sediment-hosted gold deposits indicate a magmatic-hydrothermal origin of the Carlin ore trend. *Geology* 44, 1015–1018.
- Lecumberri-Sanchez, P., Steele-MacInnis, M., Bodnar, R.J., 2012. A numerical model to estimate trapping conditions of fluid inclusions that homogenize by halite disappearance. *Geochim. Cosmochim. Acta* 92, 14–22.

- Liu, X., Yang, K.F., Rusk, B., Qiu, Z.J., Hu, F.F., Pironon, J., 2019. Copper Sulfide Remobilization and Mineralization during Paleoproterozoic Retrograde Metamorphism in the Tongkuangyu Copper Deposit, North China Craton. *Minerals* 9, 443.
- Liu, X., Fan, H.R., Yang, K.F., Qiu, Z.J., Hu, F.F., Zhu, X.Y., 2016. Geochronology, redox-state and origin of the ore-hosting porphyry in the Tongkuangyu Cu deposit, North China Craton: Implications for metallogenesis and tectonic evolution. *Precambrian Res.* 276, 211–232.
- Liu, X., Fan, H.R., Qiu, Z.J., Yang, K.F., Hu, F.F., Guo, S.L., Zhao, F.C., 2015. Formation ages of the Jiangxian and Zhongtiao Groups in the Zhongtiao Mountain region, North China craton: Insights from SIMS U-Pb dating on zircons of intercalated plagioclase amphibolites. *Acta Petrol. Sin.* 31, 1564–1572 (in Chinese with English abstract).
- Lu, J., Chen, W., Jiang, S.Y., Zhao, K.D., Simonetti, A., Pia, D.H., 2021. In-situ Sulfur Isotopic Analysis of Sulfate by Laser Ablation Multiple Collector Inductively Coupled Plasma Mass Spectrometry (LA-MC-ICP-MS). *At. Spectrosc.* 41, 223–233.
- Meng, X., Richards, J., Mao, J., Ye, H., DuFrane, S.A., Creaser, R., Marsh, J., Petrus, J., 2020. The Tongkuangyu Cu Deposit, Trans-North China Orogen: A Metamorphosed Paleoproterozoic Porphyry Cu Deposit. *Econ. Geol.* 115, 51–77.
- Morrissey, L.J., Tomkins, A.G., 2020. Evaporite-bearing orogenic belts produce ligand-rich and diverse metamorphic fluids. *Geochim. Cosmochim. Acta* 275, 163–187.
- Oliver, N.H.S., 1996. Review and classification of structural controls on fluid flow during regional metamorphism. *J. Metamorph. Geol.* 14, 477–492.
- Pichavant, M., Ramboz, C., Weisbrod, A., 1982. Fluid immiscibility in natural processes: use and misuse of fluid inclusion data: I. Phase equilibria analysis—a theoretical and geometrical approach. *Chem. Geol.* 37, 1–27.
- Peng, P., Wang, X.P., Windley, B.F., Guo, J.H., Zhai, M.G., Li, Y., 2014. Spatial distribution of ~1950–1800 Ma metamorphic events in the North China Craton: implications for tectonic subdivisions of the craton. *Lithos* 202–203, 250–266.
- Phillips, G.N., Powell, R., 2010. Formation of gold deposits: a metamorphic devolatilization model. *J. Metamorph. Geol.* 28, 689–718.
- Qiu, Z.J., Fan, H.R., Liu, X., Wen, B.J., Hu, F.F., Yang, K.F., Guo, S.L., Zhao, F.C., 2015. Fluid Inclusion and Carbon-Oxygen Isotope Studies of the Huijiayu Cu Deposit, Zhongtiao Mountains, China: Implications for Syn-metamorphic Copper Remobilization. *Acta Geol. Sin.* 89, 726–745.
- Qiu, Z.J., Fan, H.R., Liu, X., Yang, K.F., Hu, F.F., Cai, Y.C., 2017. Metamorphic PTt evolution of Paleoproterozoic schist-hosted Cu deposits in the Zhongtiao Mountains, North China Craton: Retrograde ore formation during sluggish exhumation. *Precambrian Res.* 300, 59–77.
- Qiu, Z.J., Fan, H.R., Liu, X., Yang, K.F., Hu, F.F., Xu, W.G., Wen, B.J., 2016. Mineralogy, chalcopyrite Re-Os geochronology and sulfur isotope of the Huijiayu Cu deposit in the Zhongtiao Mountains, North China Craton: Implications for a Paleoproterozoic metamorphogenic copper mineralization. *Ore Geol. Rev.* 78, 252–267.
- Qiu, Z., Fan, H.R., Tomkins, A., Brugger, J., Etschmann, B., Liu, X., Xing, Y., Hu, Y., 2021a. Insights into salty metamorphic fluid evolution from scapolite in the Trans-North China Orogen: Implication for ore genesis. *Geochim. Cosmochim. Acta* 293, 256–276.
- Qiu, Z., Fan, H.R., Goldfarb, R., Tomkins, A.G., Yang, K.F., Li, X., Xie, L.W., Liu, X., 2021b. Cobalt concentration in a sulfidic sea and mobilization during orogenesis: Implications for targeting epigenetic sediment-hosted Cu-Co deposits. *Geochim. Cosmochim. Acta* 304, 1–18.
- Ramboz, C., Pichavant, M., Weisbrod, A., 1982. Fluid immiscibility in natural processes: Use and misuse of fluid inclusion data: II. Interpretation of fluid inclusion data in terms of immiscibility. *Chem. Geol.* 37, 29–48.
- Ridley, J.R., Diamond, L.W., 2000. Fluid chemistry of lode-gold deposits and implications for genetic models. In: Hagemann S.G., Brown P. (Eds.), *Gold in 2000*. *Rev. Econ. Geol.* 13, 141–162.
- Rusk, B.G., Reed, M.H., Dilles, J.H., Klemm, L.M., Heinrich, C.A., 2004. Compositions of magmatic hydrothermal fluids determined by LA-ICP-MS of fluid inclusions from the porphyry copper-molybdenum deposit at Butte. *MT. Chem. Geol.* 210, 173–199.
- Santosh, M., 2010. Assembling North China Craton within the Columbia supercontinent: the role of double-sided subduction. *Precambrian Res.* 178, 149–167.
- Selley, D., Broughton, D., Scott, R. J., Hitzman, M., Bull, S.W., Large, R.R., McGoldrick, P. J., Croaker, M., Pollington, N., 2005. A new look at the geology of the Zambian Copperbelt. *Soc. Econ. Geol., Inc.*, 100.
- Seward, T., Williams-Jones, A., Migdisov, A., 2014. The chemistry of metal transport and deposition by ore-forming hydrothermal fluids. *Treatise Geochem.* 13, 29–57.
- Sillitoe, R.H., 2010. Porphyry copper systems. *Econ. Geol.* 105, 3–41.
- Sillitoe, R.H., Perelló, J., Creaser, R.A., Wilton, J., Wilson, A.J., Dawborn, T., 2017. Age of the Zambian Copperbelt. *Miner. Deposita* 52, 1245–1268.
- Stern, S.M., Bodnar, R.J., 1991. Synthetic fluid inclusions; X, Experimental determination of PVTX properties in the CO₂-H₂O system to 6 kb and 700 degrees C. *Am. J. Sci.* 291, 1–54.
- Sun, D.Z., Hu, W.X., Tang, M., Zhao, F.Q., Condie, K.C., 1990. Origin of Late Archean and Early Proterozoic rocks and associated mineral deposits from the Zhongtiao Mountains, east-central China. *Precambrian Res.* 47, 287–306.
- Tang, L., Santosh, M., 2018. Neoproterozoic-Paleoproterozoic terrane assembly and Wilson cycle in the North China Craton: an overview from the central segment of the Trans-North China Orogen. *Earth Sci. Rev.* 182, 1–27.
- Tian, W., Liu, S.W., Zhang, H.F., 2006. Paleoproterozoic potassic granitoids in the Sushui complex from the Zhongtiao Mountains, Northern China: geochronology, geochemistry and petrogenesis. *Acta Geol. Sin.* 80, 875–885.
- Trap, P., Faure, M., Lin, W., Monié, P., 2007. Late Paleoproterozoic (1900–1800 Ma) nappe stacking and polyphase deformation in the Hengshan-Wutaishan area: implications for the understanding of the Trans-North-China Belt, North China Craton. *Precambrian Res.* 156, 85–106.
- Turlin, F., Eglinger, A., Vanderhaeghe, O., André-Mayer, A.S., Poujol, M., Mercadier, J., Bartlett, R., 2016. Synmetamorphic Cu remobilization during the Pan-African orogeny: Microstructural, petrological and geochronological data on the kyanite-micaschists hosting the Cu (-U) Lumwana deposit in the Western Zambian Copperbelt of the Lufilian belt. *Ore Geol. Rev.* 75, 52–75.
- Warren, J.K., 2016. *Evaporites: A Geological Compendium*. Springer International Publishing Switzerland. 1–1783.
- Williams-Jones, A.E., Samson, I.M., Ault, K.M., Gagnon, J.E., Fryer, B.J., 2010. The genesis of distal zinc skarns: Evidence from the Mochito deposit, Honduras. *Econ. Geol.* 105, 1411–1440.
- Yardley, B.W., Cleverley, J.S., 2015. The role of metamorphic fluids in the formation of ore deposits. *Geol. Soc. Lond. Special Publications* 393, 117–134.
- Yardley, B.W.D., 2005. Metal concentrations in crustal fluids and their relationship to ore formation. *Econ. Geol.* 100, 613–632.
- Yardley, B.W.D., Bodnar, R.J., 2014. Fluids in the continental crust. *Geochem. Perspect.* 3, 1–2.
- Zhai, M., Santosh, M., 2013. Metallogeny of the North China Craton: link with secular changes in the evolving Earth. *Gondwana Res.* 24, 275–297.
- Zhang, X.N., Li, G.M., Qin, K.Z., Lehmann, B., Li, J.X., Zhao, J.X., 2020. Porphyry to epithermal transition at the Rongna Cu-(Au) deposit, Tibet: Insights from HO isotopes and fluid inclusion analysis. *Ore Geol. Rev.* 123, 103585.
- Zhao, G.C., Zhai, M.G., 2013. Lithotectonic elements of Precambrian basement in the North China Craton: review and tectonic implications. *Gondwana Res.* 23, 1207–1240.
- Zhao, G.C., Sun, M., Wilde, S.A., Li, S.Z., 2005. Late Archean to Paleoproterozoic evolution of the North China Craton: key issues revisited. *Precambrian Res.* 136, 177–202.
- Zhong, R., Brugger, J., Tomkins, A.G., Chen, Y., Li, W., 2015. Fate of gold and base metals during metamorphic devolatilization of a pelite. *Geochim. Cosmochim. Acta* 171, 338–352.
- Zhu, Z.Y., Cook, N.J., Yang, T., Ciobanu, C.L., Zhao, K.D., Jiang, S.Y., 2016. Mapping of sulfur isotopes and trace elements in sulfides by LA-(MC)-ICP-MS: potential analytical problems, improvements and implications. *Minerals* 6, 110.